Journal of Computational Physics 228 (2009) 2739–2757

Contents lists available at ScienceDirect

Journal of Computational Physics

journal homepage: www.elsevier.com/locate/jcp

Nonlinear magnetohydrodynamics in axisymmetric heterogeneous domains using a Fourier/finite element technique and an interior penalty method

J.-L. Guermond [a,*,1], R. Laguerre [a,b,f], J. Léorat [c], C. Nore [b,d,e]

[a] Department of Mathematics, Texas A&M University, 3368 TAMU, College Station, TX 77843-3368, USA
[b] Laboratoire d'Informatique pour la Mécanique et les Sciences de l'Ingénieur, CNRS, BP 133, 91403 Orsay cedex, France
[c] Luth, Observatoire de Paris-Meudon, place Janssen, 92195-Meudon, France
[d] Université Paris Sud 11, Département de Physique, 91405 Orsay cedex, France
[e] Institut Universitaire de France, France
[f] Université Libre de Bruxelles, CP231, Boulevard du Triomphe, Bruxelles-1050, Belgium

ARTICLE INFO

Article history:
Received 5 June 2008
Received in revised form 5 December 2008
Accepted 8 December 2008
Available online 30 December 2008

MSC:
65N30
76E25
76W05

Keywords:
Finite elements
Discontinuous Galerkin
Magnetohydrodynamics
Nonlinear dynamo action

ABSTRACT

The Maxwell equations in the MHD limit in heterogeneous axisymmetric domains composed of conducting and non-conducting regions are solved by using a mixed Fourier/Lagrange finite element technique. Finite elements are used in the meridian plane and Fourier modes are used in the azimuthal direction. Parallelization is made with respect to the Fourier modes. Continuity conditions across interfaces are enforced using an interior penalty technique. The performance of the method is illustrated on kinematic and full dynamo configurations.

© 2008 Elsevier Inc. All rights reserved.

1. Introduction

The purpose of this paper is to describe a numerical technique for solving the magnetohydrodynamic (MHD) equations in heterogeneous axisymmetric domains. The MHD approximation provides the simplest description of the dynamical coupling between matter (described as a fluid) and the electromagnetic field. Denoting by $\mathcal{U}$ the characteristic hydrodynamic velocity scale, the MHD limit we refer to corresponds to $\mathcal{U} \ll c$, where c is the speed of light. In this context, the displacement currents are neglected and the electromagnetic waves are filtered out. We refer to [2,8] for the asymptotic analysis of this problem. We particularly focus our attention on domains that can be decomposed into regions with nonzero conductivity and regions

* Corresponding author.
E-mail addresses: guermond@limsi.fr, guermond@math.tamu.edu (J.-L. Guermond), rlaguerr@ulb.ac.be (R. Laguerre), Jacques.Leorat@obspm.fr (J. Léorat), nore@limsi.fr (C. Nore).

[1] On long leave from LIMSI (CNRS-UPR 3251), BP 133, 91403, Orsay, France. This author is supported in part by the National Science Foundation Grants DMS-0510650, DMS-0713829.

0021-9991/$ - see front matter © 2008 Elsevier Inc. All rights reserved.
doi:10.1016/j.jcp.2008.12.026

with zero conductivity. Moreover, the conducting regions can be decomposed into solid and fluid parts. Fulfilling the continuity conditions of the magnetic field across interfaces between media of different conductivities, including insulators, is an obstacle for analytical and numerical methods. The main application we have in mind is the dynamo action in the laboratory or in astrophysical objects. We particularly focus our attention on axisymmetric domains, which are of widespread interest.

This work is the follow-up of [21] where we described a technique for solving the Maxwell part of the problem. In the present work, we address the full problem, i.e., that of solving the Navier–Stokes and the Maxwell equations simultaneously in realistic heterogeneous configurations. To benefit from the axisymmetry of the domain, we use finite elements in the meridian plane and Fourier modes in the azimuthal direction in the spirit of [31,33,21]. Parallelization is made with respect to the Fourier modes. Continuity and other transmission conditions across interfaces are enforced using an interior penalty technique à la Nitsche [28] and Dupont–Douglas [14]. The main originality of the technique is that it can handle heterogeneous media.

The performance of the code is evaluated on various test cases. We present calculations of hydrodynamic and hydromagnetic instabilities in a periodic setting and a finite Taylor–Couette configuration. The Taylor–Couette flow is used in kinematic dynamo computations and a Hopf bifurcation towards a magnetic structure of typical length scale twice that of the velocity field is discovered. The nonlinear dynamo regime is studied as well. Periodic and no-slip boundary conditions are shown to give rise to very different behaviors, thus shedding some doubts on the relevance of dynamo computations done assuming periodicity or other *ad hoc* boundary conditions.

The paper is organized as follows. We introduce the setting and a weak formulation of the problem under consideration in Section 2. The discretization technique is described in Section 3, where we give details on the time and space discretization, on the parallelization and on the interior penalty approximation technique. Section 4 focuses on validation tests involving a kinematic and a full dynamo. Concluding remarks are reported in Section 5.

2. The continuous problem

2.1. The geometric setting

Let us consider a bounded domain $\Omega \subset \mathbb{R}^3$. The boundary of Ω is denoted by $\Gamma = \partial\Omega$ and is henceforth assumed to be at least Lipschitz continuous. Ω is assumed to be partitioned into a conducting region (subscript c) and an insulating region (subscript v) as follows:

$$\overline{\Omega} = \overline{\Omega}_c \cup \overline{\Omega}_v, \quad \Omega_c \cap \Omega_v = \emptyset. \tag{2.1}$$

Ω_c is referred to as the conducting domain and Ω_v is referred to as the non-conducting domain. The conducting domain is further assumed to be partitioned into a fluid region Ω_{cf} and a solid region Ω_{cs}:

$$\overline{\Omega_c} = \overline{\Omega_{cs}} \cup \overline{\Omega_{cf}}, \quad \Omega_{cs} \cap \Omega_{cf} = \emptyset. \tag{2.2}$$

The interface between the conducting region and the non-conducting region is denoted by

$$\Sigma = \partial\Omega_c \cap \partial\Omega_v. \tag{2.3}$$

To easily refer to boundary conditions, we introduce

$$\Gamma_c = \Gamma \cap \partial\Omega_c, \quad \Gamma_v = \Gamma \cap \partial\Omega_v, \quad \Gamma_f = \partial\Omega_{cf}. \tag{2.4}$$

Note that $\Gamma = \Gamma_v \cup \Gamma_c$. Moreover, we denote by Γ_v^0 the connected component of $\partial\Omega_v$ that contains Γ_v. We assume that $\partial\Omega_v$ has $J+1$ connected components, say

$$\Gamma_v^0, \Gamma_v^1, \ldots, \Gamma_v^J. \tag{2.5}$$

Observe that $\Sigma = (\Gamma_v^0 \setminus \Gamma_v) \cup \Gamma_v^1 \cup \cdots \cup \Gamma_v^J$.

The notation is illustrated in Fig. 1 on two examples. The vertical dashed line represents the symmetry axis. Only the meridian section of each region is shown. For the setting in the left panel (a) we have $J = 2$ (3 conducting torii) and $\Sigma = (\Gamma_v^0 \setminus \Gamma_v) \cup \Gamma_v^1 \cup \Gamma_v^2$. For the domain in the right panel (b) we have $J = 1$, $\Gamma_v^0 = \Gamma_v$, $\Gamma_c = \emptyset$ and $\Sigma = \Gamma_v^1$.

2.2. The PDE setting

The time evolution of the fluid occupying Ω_{cf} is modeled by the incompressible Navier–Stokes equations and the electromagnetic field in Ω is modeled by the Maxwell equations in the MHD limit. The conducting fluid and the electromagnetic field interact through the Lorentz force. The set of equations describing the situation is the following:

$$\begin{cases} \partial_t \mathbf{u} + (\mathbf{u}\cdot\nabla)\mathbf{u} - \nu\Delta\mathbf{u} + \frac{1}{\rho}\nabla p = \frac{1}{\rho}(\nabla\times\mathbf{H})\times\mu\mathbf{H} \quad \text{in } \Omega_{cf}, \\ \nabla\cdot\mathbf{u} = 0 \quad \text{in } \Omega_{cf}, \\ \mathbf{u}|_{t=0} = \mathbf{u}_0 \text{ in } \Omega_{cf}, \quad \mathbf{u}|_{\Gamma_f} = \mathbf{d}, \end{cases} \tag{2.6}$$

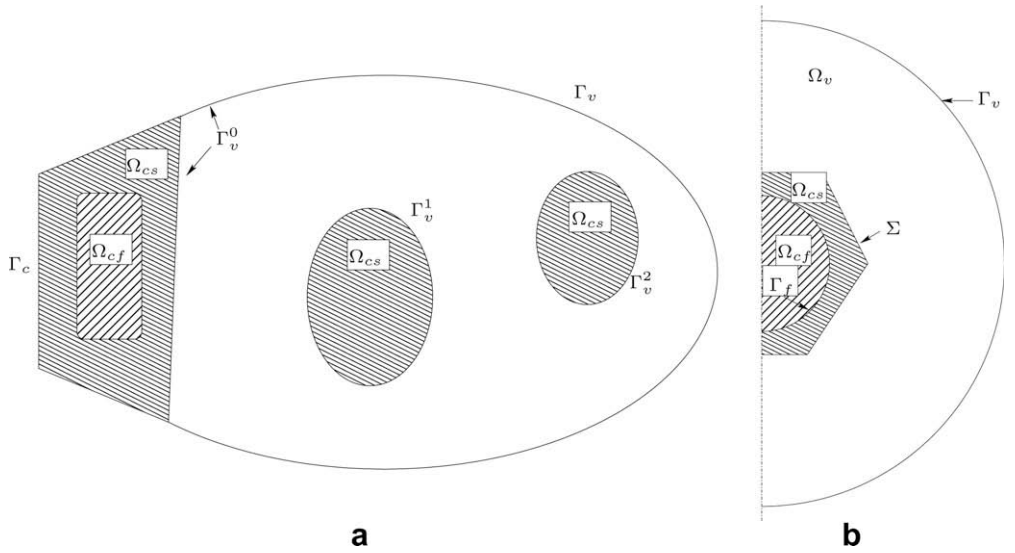

Fig. 1. Two examples of computational domains Ω with various boundaries. The shaded regions constitute the conducting domain Ω_c, the non-shaded domain is vacuum Ω_v.

$$\begin{cases} \mu\partial_t \mathbf{H} = -\nabla\times\mathbf{E} \quad \text{in } \Omega \\ \nabla\times\mathbf{H} = \begin{cases} \sigma(\mathbf{E}+\tilde{\mathbf{u}}\times\mu\mathbf{H})+\mathbf{j}^s & \text{in } \Omega_c, \\ 0 \quad \text{in } \Omega_v, \end{cases} \\ \nabla\cdot\mathbf{E} = 0 \quad \text{in } \Omega_v \\ \mathbf{E}\times\mathbf{n}|_\Gamma = \mathbf{a}, \quad \mathbf{H}|_{t=0} = \mathbf{H}_0 \text{ in } \Omega, \\ \int_{\Gamma_v^i} \mathbf{E}\cdot\mathbf{n} = 0, \quad 1 \leqslant i \leqslant J, \end{cases} \tag{2.7}$$

where $\mathbf{n}$ is the outward normal on Γ. For the sake of simplicity of the presentation we consider only the natural boundary condition $\mathbf{E}\times\mathbf{n}|_\Gamma = \mathbf{a}$ for the time being. An essential boundary condition $\mathbf{H}\times\mathbf{n}|_\Gamma = \mathbf{a}$ can be imposed as an alternative; we refer to Section 2.5 for more details on boundary conditions.

The independent variables are space and time. The dependent variables are the velocity field of the fluid, $\mathbf{u}$, the pressure in the fluid, p, the magnetic field, $\mathbf{H}$ and the electric field, $\mathbf{E}$. The quantity $\tilde{\mathbf{u}}$ is an extension of $\mathbf{u}$ on Ω_c, i.e., $\tilde{\mathbf{u}}$ is equal to $\mathbf{u}$ on Ω_{cf} and is prescribed in Ω_{cs}. It is common to set $\tilde{\mathbf{u}}$ to zero in Ω_{cs}, but if some parts of the solid are rotating about the symmetry axis $\tilde{\mathbf{u}}$ is prescribed to be equal to the solid rotation velocity in the regions that rotate. The data are $\mathbf{u}_0$, $\mathbf{H}_0$, $\mathbf{d}$, $\mathbf{a}$ and $\mathbf{j}^s$: $\mathbf{u}_0$ and $\mathbf{H}_0$ are initial conditions; $\mathbf{d}$ and $\mathbf{a}$ are boundary data; $\mathbf{j}^s$ is an externally imposed distribution of current. The data are assumed to satisfy all the usual compatibility conditions, i.e., $\nabla\cdot(\mu\mathbf{H}_0) = 0$, $\nabla\cdot\mathbf{u}_0 = 0$, $\mathbf{u}_0|_{\Gamma_f} = \mathbf{d}|_{t=0}$, etc. The physical parameters are the kinematic viscosity ν, the fluid density, ρ, the magnetic permeability, μ and the conductivity, σ; ν and ρ are constant, whereas μ and σ depend on space and μ is smooth.

In the above formulation the displacement currents represented by the term $\epsilon\partial_t\mathbf{E}$ in the Ampère–Maxwell equation have been neglected due to the fact that $\mathbf{u}$ scales like $\mathcal{U}$, where the scale of interest $\mathcal{U}$ is such that $\mathcal{U}/\mathfrak{c}$ is extremely small.

Observe that the conditions $\nabla\cdot\mathbf{E}|_{\Omega_v} = 0$ and $\int_{\Gamma_v^i}\mathbf{E}\cdot\mathbf{n} = 0$, $1 \leqslant i \leqslant J$ are what is left from the Ampère–Maxwell equation when passing to the limit to zero on the ratio $\mathcal{U}/\mathfrak{c}$ assuming that there is no electrostatic charge distributed in the domain. These extra conditions ensure that $\mathbf{E}$ is uniquely defined, i.e., they have no effect on $\mathbf{H}$. Note that the condition $\int_{\Gamma_v^0}\mathbf{E}\cdot\mathbf{n} = 0$ need not be enforced since it is a consequence of the J other conditions together with $\mathbf{E}$ being solenoidal. We refer to [8,2] for more details on the asymptotic analysis leading to (2.7).

When σ is uniformly positive over Ω, i.e., $\Omega_c = \Omega$, an evolution equation for $\mathbf{H}$ can be obtained after eliminating the electric field. This short cut is no longer possible when Ω_v is non-trivial and determining the complete solution, including the electric field, is no longer straightforward.

We henceforth assume that the conductivity $\sigma(\mathbf{x})$ is zero in Ω_v and is bounded from below and from above in Ω_c by positive constants. We also assume that the restrictions of $\mu(\mathbf{x})$ to Ω_c and Ω_v are smooth functions, respectively; i.e., μ can be discontinuous across the interface Σ. We are currently developing a technique to account for discontinuities of μ in the conductors.

2.3. Non-dimensionalization of the equations

We now non-dimensionalize the problem. We denote by $\mathcal{L}$ and $\mathcal{U}$ the reference length and velocity scales, respectively. Our basic assumption is that $\mathcal{U} \ll \mathfrak{c}$, where $\mathfrak{c}$ is the speed of light. The reference (advective) time scale is $\mathcal{T} := \mathcal{L}/\mathcal{U}$. The fluid

density is assumed to be a constant ρ and the reference pressure scale is $\mathcal{P} := \rho\mathcal{U}^2$. The reference magnetic permeability and electric conductivity are denoted by μ_0 and σ_0, respectively. We choose the reference scale for the magnetic field to be so that the reference Alfvén speed is one, i.e., $\mathcal{H} := \mathcal{U}\sqrt{\rho/\mu_0}$. The reference scale for the electric field is set to be $\mathcal{E} := \mu_0\mathcal{H}\mathcal{U}$. The source current $\mathbf{j}^s$ and the data $\mathbf{u}_0$, $\mathbf{d}$, $\mathbf{H}_0$, $\mathbf{a}$ are non-dimensionalized by $\mathcal{H}\mathcal{L}^{-1}$, $\mathcal{U}$, $\mathcal{U}$, $\mathcal{H}$ and $\mathcal{H}$, respectively. We are left with two non-dimensional parameters which we refer to as the dynamic Reynolds number, R_e and the magnetic Reynolds number, R_m, which are defined as follows:

$$R_e := \frac{\mathcal{U}\mathcal{L}}{\nu}, \quad R_m := \mathcal{U}\mathcal{L}\sigma_0\mu_0. \tag{2.8}$$

Henceforth we abuse the notation by using the same symbols for the non-dimensional and the corresponding dimensional quantities. The non-dimensional set of equations is as follows:

$$\begin{cases} \partial_t\mathbf{u} + (\mathbf{u}\cdot\nabla)\mathbf{u} - R_e^{-1}\Delta\mathbf{u} + \nabla p = (\nabla\times\mathbf{H})\times\mu\mathbf{H} & \text{in } \Omega_{cf}, \\ \nabla\cdot\mathbf{u} = 0 \quad \text{in } \Omega_{cf}, \\ \mathbf{u}|_{t=0} = \mathbf{u}_0 \quad \text{in } \Omega_{cf}, \quad \mathbf{u}|_{\Gamma_f} = \mathbf{d}, \end{cases} \tag{2.9}$$

$$\begin{cases} \mu\partial_t\mathbf{H} = -\nabla\times\mathbf{E} \quad \text{in } \Omega, \\ \nabla\times\mathbf{H} = \begin{cases} R_m\sigma(\mathbf{E} + \tilde{\mathbf{u}}\times\mu\mathbf{H}) + \mathbf{j}^s & \text{in } \Omega_c, \\ 0 & \text{in } \Omega_v, \end{cases} \\ \nabla\cdot\mathbf{E} = 0 \quad \text{in } \Omega_v, \\ \mathbf{E}\times\mathbf{n}|_\Gamma = \mathbf{a}, \quad \mathbf{H}|_{t=0} = \mathbf{H}_0 \quad \text{in } \Omega, \\ \int_{\Gamma_v^i}\mathbf{E}\cdot\mathbf{n} = 0, \quad 1 \leqslant i \leqslant J, \end{cases} \tag{2.10}$$

where σ and μ are the relative conductivity and permeability, respectively.

2.4. Introduction of ϕ and elimination of $\mathbf{E}$

In addition to the above hypotheses on Ω, we henceforth assume that the initial data $\mathbf{H}_0$ is such that $\nabla\times\mathbf{H}_0|_{\Omega_v} = 0$. We also assume that either Ω_v is simply connected or there is some mechanism that ensures that the circulation of $\mathbf{H}$ along any path in the insulating media is zero. The condition $\nabla\times\mathbf{H}|_{\Omega_v} = 0$ then implies that there is a scalar potential ϕ, defined up to an arbitrary constant, such that $\mathbf{H}|_{\Omega_v} = \nabla\phi$. Moreover, we can also define ϕ_0 such that $\mathbf{H}_0|_{\Omega_v} = \nabla\phi_0$. We now define

$$\mathbf{H} = \begin{cases} \mathbf{H}^c & \text{in } \Omega_c, \\ \nabla\phi & \text{in } \Omega_v, \end{cases} \quad \mu = \begin{cases} \mu^c & \text{in } \Omega_c, \\ \mu^v & \text{in } \Omega_v \end{cases} \tag{2.11}$$

and we denote by $\mathbf{n}^c$ and $\mathbf{n}^v$ the outward normal on $\partial\Omega_c$ and $\partial\Omega_v$, respectively. It is possible to eliminate the electric field from the problem (see e.g. [21] for the details) and we finally obtain:

$$\begin{cases} \mu^c\partial_t\mathbf{H}^c = -\nabla\times(R_m^{-1}\sigma^{-1}(\nabla\times\mathbf{H}^c - \mathbf{j}^s) - \tilde{\mathbf{u}}\times\mu^c\mathbf{H}^c) & \text{in } \Omega_c, \\ \mu^v\partial_t\Delta\phi = 0 & \text{in } \Omega_v, \\ (R_m^{-1}\sigma^{-1}(\nabla\times\mathbf{H}^c - \mathbf{j}^s) - \tilde{\mathbf{u}}\times\mu^c\mathbf{H}^c)\times\mathbf{n}^c = \mathbf{a} & \text{on } \Gamma_c, \\ \mu^v\partial_{\mathbf{n}^v}(\partial_t\phi) = -\mathbf{n}^v\cdot\nabla\times(\mathbf{n}^v\times\mathbf{a}) & \text{on } \Gamma_v, \\ \mathbf{H}^c\times\mathbf{n}^c + \nabla\phi\times\mathbf{n}^v = 0 & \text{on } \Sigma, \\ \mu^c\mathbf{H}^c\cdot\mathbf{n}^c + \mu^v\nabla\phi\cdot\mathbf{n}^v = 0 & \text{on } \Sigma, \\ \mathbf{H}^c|_{t=0} = \mathbf{H}_0^c, \quad \phi|_{t=0} = \phi_0. \end{cases} \tag{2.12}$$

Observe that the operator $\mathbf{n}^v\cdot\nabla\times(\cdot)$ involves only tangential derivatives; hence, it is meaningful to have it acting on the field $\mathbf{n}^v\times\mathbf{a}$ which is only defined on Γ. Note also that $(\mu^c\mathbf{H}^c\cdot\mathbf{n}^c + \mu^v\nabla\phi\cdot\mathbf{n}^v)|_\Sigma = 0$ expresses the continuity of the normal component of the magnetic induction across Σ. This equation is a consequence of the continuity of the tangential component of the electric field. If the electric field is needed, it is computed in the conducting domain by using Ohm's law and it is determined in the non-conducting medium by solving the Cauchy–Riemann problem: $\nabla\times\mathbf{E}^v = -\mu^v\partial_t\nabla\phi$, $\nabla\cdot\mathbf{E}^v = 0$, $\mathbf{E}^v\times\mathbf{n}^v|_\Sigma = -\mathbf{E}^c\times\mathbf{n}^c|_\Sigma$, $\mathbf{E}^v\times\mathbf{n}^v|_{\Gamma_v} = \mathbf{a}$ and $\int_{\Gamma_v^i}\mathbf{E}^v\cdot\mathbf{n}^v = 0$, $1 \leqslant i \leqslant J$. Note that (2.12) does not involve the Γ_v^i's, $1 \leqslant i \leqslant J$.

2.5. Weak formulation

Finding a weak formulation of the Navier–Stokes equations does not pose any particular difficulty, see e.g. [36]. We define the Hilbert spaces

$$\mathbf{H}^1(\Omega_{cf}) = \left\{\mathbf{v}\in\mathbf{L}^2(\Omega_{cf}), \nabla\mathbf{v}\in\mathbf{L}^2(\Omega_{cf})\right\}, \tag{2.13}$$

$$L^2_{\int=0}(\Omega_{cf}) = \left\{ q \in L^2(\Omega_{cf}),\ \int_{\Omega_{cf}} q = 0 \right\}, \tag{2.14}$$

$$\mathbf{H}^1_0(\Omega_{cf}) = \left\{ \mathbf{v} \in \mathbf{H}^1(\Omega_{cf}),\ \mathbf{v}|_{\Gamma_f} = \mathbf{0} \right\}, \tag{2.15}$$

equipped with the canonical norms. The Navier–Stokes problem then consists of finding $\mathbf{u} \in L^2((0,+\infty);\mathbf{H}^1(\Omega_{cf}))$ and $p \in L^2((0,+\infty);L^2_{\int=0}(\Omega))$ (with the time derivative of $\mathbf{u}$ in an appropriate space [36]) so that $\mathbf{u}|_{t=0} = \mathbf{u}_0$, $\mathbf{u}|_{\Gamma_f} = \mathbf{d}$ and for all $(\mathbf{v},q) \in \mathbf{H}^1_0(\Omega_{cf}) \times L^2_{\int=0}(\Omega)$ and for almost every $t \in (0,+\infty)$,

$$\begin{cases} \int_{\Omega_{cf}} \left[(\partial_t \mathbf{u} + \mathbf{u}\cdot\nabla\mathbf{u} + \nabla p)\cdot\mathbf{v} + R_e^{-1}\nabla\mathbf{u} : \nabla\mathbf{v} \right] = \int_{\Omega_{cf}} ((\nabla\times\mathbf{H}^c)\times\mu\mathbf{H}^c)\cdot\mathbf{v}, \\ \int_{\Omega_{cf}} q\nabla\cdot\mathbf{u} = 0. \end{cases} \tag{2.16}$$

We have defined $\nabla\mathbf{u} : \nabla\mathbf{v} = \sum_{ij}\partial_i u_j \partial_i v_j$. Existence of weak solutions to this problem when $\mathbf{H}^c$ is prescribed and sufficiently smooth is known, see e.g. [36].

The weak formulation of (2.10) that we want to use has been derived in [21]. We introduce the following spaces:

$$\mathbf{L} = \left\{ (\mathbf{b},\varphi) \in \mathbf{L}^2(\Omega_c) \times H^1_{\int=0}(\Omega_v) \right\}, \tag{2.17}$$

$$\mathbf{X} = \left\{ (\mathbf{b},\varphi) \in \mathbf{H}_{\mathrm{curl}}(\Omega_c) \times H^1_{\int=0}(\Omega_v);\ (\mathbf{b}\times\mathbf{n}^c + \nabla\varphi\times\mathbf{n}^v)|_\Sigma = 0 \right\} \tag{2.18}$$

and we equip $\mathbf{L}$ and $\mathbf{X}$ with the norm of $\mathbf{L}^2(\Omega_c)\times H^1(\Omega_v)$ and $\mathbf{H}_{\mathrm{curl}}(\Omega_c)\times H^1(\Omega_v)$, respectively. $H^1_{\int=0}(\Omega_v)$ is the subspace of $H^1(\Omega_v)$ composed of the functions of zero mean value. The space $\mathbf{H}_{\mathrm{curl}}(\Omega_c)$ is composed of the vector-valued functions on Ω_c that are componentwise L^2-integrable and whose curl is also componentwise L^2-integrable. The space $\mathbf{H}_{\mathrm{div}}(\Omega)$ is composed of the vector-valued functions on Ω that are componentwise L^2-integrable and whose divergence is L^2-integrable.

We are now in position to formulate the problem as follows: Seek the pair $(\mathbf{H}^c,\phi) \in L^2((0,+\infty);\mathbf{X}) \cap L^\infty((0,+\infty);\mathbf{L})$ (with $\partial_t\mathbf{H}^c$ and $\partial_t\phi$ in appropriate spaces) such that for all $(\mathbf{b},\varphi)\in\mathbf{X}$ and for almost every $t\in(0,+\infty)$,

$$\begin{cases} \mathbf{H}^c|_{t=0} = \mathbf{H}^c_0; \quad \nabla\phi|_{t=0} = \nabla\phi_0, \\ \int_{\Omega_c}\left[\mu^c(\partial_t\mathbf{H}^c)\cdot\mathbf{b} + ((R_m\sigma)^{-1}(\nabla\times\mathbf{H}^c - \mathbf{j}^s) - \tilde{\mathbf{u}}\times\mu^c\mathbf{H}^c)\cdot\nabla\times\mathbf{b}\right] + \int_{\Omega_v}\mu^v(\partial_t\nabla\phi)\cdot\nabla\varphi \\ \quad + \int_\Sigma((R_m\sigma)^{-1}(\nabla\times\mathbf{H}^c - \mathbf{j}^s) - \tilde{\mathbf{u}}\times\mu^c\mathbf{H}^c)\cdot(\mathbf{b}\times\mathbf{n}^c + \nabla\varphi\times\mathbf{n}^v) \\ \quad = \int_{\Gamma_c}(\mathbf{a}\times\mathbf{n})\cdot(\mathbf{b}\times\mathbf{n}) + \int_{\Gamma_v}(\mathbf{a}\times\mathbf{n})\cdot(\nabla\varphi\times\mathbf{n}). \end{cases} \tag{2.19}$$

The interface integral over Σ is zero since $\mathbf{b}\times\mathbf{n}^c + \nabla\varphi\times\mathbf{n}^v = 0$, but we nevertheless retain it since it does not vanish when we construct the non-conforming finite element approximation in Section 3.

Note that since the data $\mathbf{a}$ is tangent on Γ by definition, i.e., $\mathbf{a} = \mathbf{n}\times(\mathbf{a}\times\mathbf{n})$, we have $\mathbf{a}\cdot\mathbf{b} = (\mathbf{a}\times\mathbf{n})\cdot(\mathbf{b}\times\mathbf{n})$ for every vector field $\mathbf{b}$.

It has been shown in [21] that (2.19) is equivalent to (2.12). Observe that the boundary conditions on Γ_v and Γ_c in (2.12) are enforced naturally in (2.19). The control of the boundary conditions on Γ_v is done by means of the boundary integral $\int_{\Gamma_v}(\mathbf{a}\times\mathbf{n})\cdot(\nabla\varphi\times\mathbf{n})$. Alternatively, a Dirichlet boundary condition on the magnetic field can be enforced, say $\nabla\phi\times\mathbf{n}|_{\Gamma_v} = \mathbf{a}$, by prescribing ϕ on Γ_v and requiring the test functions φ to be zero on Γ_v. Note that the boundary condition $\nabla\phi\times\mathbf{n}|_{\Gamma_v} = \mathbf{a}$ only involves the tangent component of the gradient and this component only depends on the value of ϕ on Γ_v.

The interface continuity condition $\mathbf{H}^c\times\mathbf{n}^c + \nabla\phi\times\mathbf{n}^v = 0$ is an essential condition, i.e., it is enforced in the space $\mathbf{X}$, see (2.18). One originality of the approximation technique introduced in [21] and recalled in Section 3 is to make this condition natural by using an interior penalty technique.

At this point it may not seem clear to the reader that the weak formulation (2.19) enforces the interface condition $\mu^c\mathbf{H}^c\cdot\mathbf{n}^c + \mu^v\nabla\phi\cdot\mathbf{n}^v = 0$ naturally. To see this, let us define $\mathbf{E}^c := (R_m\sigma)^{-1}(\nabla\times\mathbf{H}^c - \mathbf{j}^s) - \tilde{\mathbf{u}}\times\mu^c\mathbf{H}^c$; clearly $\nabla\times\mathbf{E}^c = -\mu^c\partial_t\mathbf{H}^c$. Let $(\mathbf{b},\varphi)$ be a smooth test function in $\mathbf{X}$ so that $\mathbf{b}$ is zero in a neighborhood of Γ_c and φ is zero in a neighborhood of Γ_v. Let $\tilde{\varphi}$ be the harmonic extension of φ on Ω defined as follows: $\tilde{\varphi} = \varphi$ in Ω_v, $\Delta\tilde{\varphi} = 0$ in Ω_c, $\tilde{\varphi}|_\Sigma = \varphi|_\Sigma$, $\tilde{\varphi}|_{\Gamma_c} = 0$. After integration by parts and using $\mathbf{b}\times\mathbf{n}^c|_{\partial\Omega_c} = \nabla\tilde{\varphi}\times\mathbf{n}^c|_{\partial\Omega_c}$, (2.19) implies

$$\begin{aligned} 0 &= -\int_\Sigma \mathbf{E}^c\cdot(\nabla\tilde{\varphi}\times\mathbf{n}^c) + \int_\Sigma\mu^v\partial_t(\nabla\phi)\cdot\mathbf{n}^v\tilde{\varphi} = \int_{\Omega_c}\nabla\times(\nabla\tilde{\varphi})\cdot\mathbf{E}^c - \int_{\Omega_c}\nabla\tilde{\varphi}\cdot(\nabla\times\mathbf{E}^c) + \int_\Sigma\mu^v\partial_t(\nabla\phi)\cdot\mathbf{n}^v\tilde{\varphi} \\ &= \int_{\Omega_c} -\nabla\cdot(\tilde{\varphi}\nabla\times\mathbf{E}^c) + \int_\Sigma\mu^v\partial_t(\nabla\phi)\cdot\mathbf{n}^v\tilde{\varphi} = \int_\Sigma(-(\nabla\times\mathbf{E}^c)\cdot\mathbf{n}^c + \mu^v\partial_t(\nabla\phi)\cdot\mathbf{n}^v)\tilde{\varphi} = d_t\int_\Sigma(\mu^c\mathbf{H}^c\cdot\mathbf{n}^c + \mu^v\nabla\phi\cdot\mathbf{n}^v)\tilde{\varphi}. \end{aligned}$$

Since $\tilde{\varphi}$ can be chosen so that $\tilde{\varphi}|_\Sigma$ is arbitrarily close to any function in $L^1(\Sigma)$, this means that $(\mu^c\mathbf{H}^c\cdot\mathbf{n}^c + \mu^v\nabla\phi\cdot\mathbf{n}^v)$ does not depend on time and space. But the compatibility condition $\nabla\cdot(\mu\mathbf{H}_0) = 0$ implies $(\mu^c\mathbf{H}^c\cdot\mathbf{n}^c + \mu^v\nabla\phi\cdot\mathbf{n}^v)|_{t=0} = 0$, meaning that $\mu^c\mathbf{H}^c\cdot\mathbf{n}^c + \mu^v\nabla\phi\cdot\mathbf{n}^v$ is zero and this condition is enforced naturally for all times.

The problem to be solved is the coupled system (2.16)–(2.19). Well-posedness of (2.19) when $\tilde{\mathbf{u}}$ is a prescribed smooth function is evident (see e.g. [2,8,21, Thm 2.1]). Existence of weak solutions of (2.16)–(2.19) is known when $\Omega = \Omega_c$, i.e., $\Omega_v = \emptyset$, see e.g. [18, Section 2.2, 32, Theorem 3.1] and uniqueness can be proved assuming smoothness. Existence of a weak solution for the fully coupled nonlinear system is not so clear when $\Omega_v \neq \emptyset$; we will nevertheless assume it in the rest of the paper.

3. Finite element approximation

We give technical implementation details in this section regarding space and time approximation of (2.16)–(2.19). We use finite elements in the meridian section and Fourier expansions in the aximuthal direction.

3.1. The geometry

We denote by Ω_v^{2D}, Ω_c^{2D} and Ω_{cf}^{2D} the meridian sections of Ω_v, Ω_c and Ω_{cf}, respectively. We assume that Ω_v^{2D}, Ω_c^{2D} and Ω_{cf}^{2D} have piecewise quadratic boundaries. These sections are meshed using quadratic triangular meshes. We denote by $\{\mathcal{F}_h^v\}_{h>0}$, $\{\mathcal{F}_h^{cs}\}_{h>0}$ and $\{\mathcal{F}_h^{cf}\}_{h>0}$ the corresponding regular families of non-overlapping quadratic triangular meshes. We assume for the sake of simplicity that for every given mesh index h, $\mathcal{F}_h^{cf}$ is a subset of $\mathcal{F}_h^c$. For every element K in the mesh $\mathcal{F}_h^v \cup \mathcal{F}_h^c$ we denote by $T_K : \widehat{K} \to K$ the quadratic transformation that maps the reference triangle $\widehat{K} := \{(\hat{r},\hat{z}) \in \mathbb{R}^2,\ 0 \leqslant \hat{r},\ 0 \leqslant \hat{z},\ \hat{r}+\hat{z} \leqslant 1\}$ to K.

We denote by Σ_h^{2D} the collection of triangle edges that compose the meridian section of Σ. The collection of cylindrical surfaces generated by rotation around the symmetry axis by the edges in Σ_h^{2D} is denoted by Σ_h. For every cylindrical surface F in Σ_h, we denote by h_F the diameter of the triangle edge that generates F.

3.2. The Fourier representation

Let (r,θ,z) be the polar coordinates and t be the time. The generic form of approximate functions is

$$f(r,\theta,z,t) = \sum_{k=-M}^{M} f_h^k(r,z,t)e^{\mathrm{i}k\theta}, \quad \mathrm{i}^2 = -1, \qquad \overline{f_h^k}(r,z,t) = f_h^{-k}(r,z,t) \quad \forall k \in \overline{0,M}, \tag{3.1}$$

where $M+1$ is the maximum number of complex Fourier modes. The coefficients $f_h^k(r,z,t)$ take values in finite element spaces defined further below.

Nothing special is enforced on the axis, i.e., at $r = 0$. Proper behaviors of approximate functions in the neighborhood of the axis are guaranteed by integration by parts and the use of the measure $r\,\mathrm{d}r\,\mathrm{d}z\,\mathrm{d}\theta$. This measure ensures that we work in the appropriate weighted Sobolev spaces; we refer to [6] for further mathematical details on weighted spaces.

3.3. Space discretization for Navier–Stokes equations

For the fluid problem we use the mixed Taylor–Hood, $\mathbb{P}_2/\mathbb{P}_1$, finite element (see e.g. [10,16,19] for details on this element). We define the finite-dimensional complex-valued vector spaces

$$\mathbf{V}_h^{2D} := \left\{\mathbf{v}_h \in \mathcal{C}^0(\overline{\Omega_{cf}}); \mathbf{v}(T_K^{-1})|_K \in \mathbb{P}_2^6\ \forall K \in \mathcal{F}_h^{cf}\right\}, \tag{3.2}$$

$$M_h^{2D} := \left\{q_h \in \mathcal{C}^0(\overline{\Omega_{cf}}); q(T_K^{-1})|_K \in \mathbb{P}_1^2\ \forall K \in \mathcal{F}_h^{cf}\right\}. \tag{3.3}$$

Then, the velocity and the pressure fields are approximated in the following spaces:

$$\mathbf{V}_h := \left\{\mathbf{v} = \sum_{k=-M}^{M} \mathbf{v}_h^k(r,z)e^{\mathrm{i}k\theta}; \mathbf{v}_h^k \in \mathbf{V}_h^{2D}, -M \leqslant k \leqslant M\right\}, \tag{3.4}$$

$$M_h := \left\{q_h = \sum_{k=-M}^{M} q_h^k(r,z)e^{\mathrm{i}k\theta}; q_h^k \in M_h^{2D}, -M \leqslant k \leqslant M\right\}. \tag{3.5}$$

We also use the notation $\mathbf{V}_{h,0}$ to denote the subspace of $\mathbf{V}_h$ composed of the vector fields that are zero on Γ_f.

3.4. Space discretization for the Maxwell equations

The electromagnetic part of the problem is approximated by using the technique introduced in [21]. The main feature is that the method is non-conforming, i.e., the continuity constraint $(\mathbf{b}\times\mathbf{n}^c + \nabla\varphi\times\mathbf{n}^v)|_\Sigma = 0$ in $\mathbf{X}$ (see (2.18)) is relaxed and enforced by means of an interior penalty method.

Let $\ell_{\mathbf{H}}$ and ℓ_ϕ be two integers in $\{1,2\}$ with $\ell_\phi \geqslant \ell_{\mathbf{H}}$. We first define the meridian finite element spaces

$$\mathbf{X}_h^{\mathbf{H},2D} := \left\{\mathbf{b}_h \in C^0(\overline{\Omega_c}); \mathbf{b}_h(T_K)|_K \in \mathbb{P}_{\ell_{\mathbf{H}}}^6,\ \forall K \in \mathcal{F}_h^c\right\}, \tag{3.6}$$

$$X_h^{\phi,2D} := \left\{\varphi_h \in \mathcal{C}^0(\overline{\Omega_v}); \varphi_h(T_K)|_K \in \mathbb{P}_{\ell_\phi}^2,\ \forall K \in \mathcal{F}_h^v\right\}. \tag{3.7}$$

Then the magnetic field and the scalar potential are approximated in the following spaces:

$$\mathbf{X}_h^{\mathbf{H}} := \left\{\mathbf{b} = \sum_{k=-M}^{M} \mathbf{b}_h^k(r,z)e^{\mathrm{i}k\theta};\ \mathbf{b}_h^k \in \mathbf{X}_h^{\mathbf{H},2D},\ -M \leqslant k \leqslant M\right\}, \tag{3.8}$$

$$X_h^\phi := \left\{ \varphi = \sum_{k=-M}^{M} \varphi_h^k(r,z) e^{ik\theta};\ \varphi_h^k \in X_h^{\phi,2D},\ -M \leqslant k \leqslant M \right\}. \tag{3.9}$$

3.5. Time discretization

We use the second-order Backward Difference Formula (BDF2) to approximate the time derivatives. The nonlinear terms are made explicit and approximated using second-order extrapolation in time; this decouples the Navier–Stokes and the Maxwell part of the problem. Let Δt be the time step and set $t^n := n\Delta t$, $n \geqslant 0$.

The velocity and pressure in the Navier–Stokes problem are decoupled by using the rotational pressure-correction method [37,23]. The nonlinear term is written in the form $(\nabla \times \mathbf{u}) \times \mathbf{u} + \frac{1}{2}\nabla \mathbf{u}^2$ and the term $\frac{1}{2}\nabla \mathbf{u}^2$ is combined with the pressure so that we work with the dynamical pressure $\pi = p + \frac{1}{2}\mathbf{u}^2$. The full algorithm is written as follows: After appropriate initialization at t^0 and t^1, for $n \geqslant 1$ set

$$\mathbf{u}^* = 2\mathbf{u}^n - \mathbf{u}^{n-1}, \quad \mathbf{H}^* = 2\mathbf{H}^{c,n} - \mathbf{H}^{c,n-1}. \tag{3.10}$$

Then solve for $\mathbf{u}^{n+1} \in \mathbf{V}_h$ so that $\mathbf{u}^{n+1}|_{\Gamma_f} = \mathbf{d}_h^{n+1}$, where $\mathbf{d}_h^{n+1}$ is an approximation of the data $\mathbf{d}(t^{n+1})$ and the following holds for all $\mathbf{v} \in \mathbf{V}_{h,0}$:

$$\int_{\Omega_{cf}} \frac{D\mathbf{u}^{n+1}}{\Delta t} \cdot \mathbf{v} + R_e^{-1} \nabla \mathbf{u}^{n+1} : \nabla \mathbf{v} = -\int_{\Omega_{cf}} \mathbf{v} \cdot \nabla \left(\pi^n + \frac{4}{3}\psi^n - \frac{1}{3}\psi^{n-1} \right) + \int_{\Omega_{cf}} \mathbf{v} \cdot ((\nabla \times \mathbf{H}^*) \times \mu \mathbf{H}^* - (\nabla \times \mathbf{u}^*) \times \mathbf{u}^*), \tag{3.11}$$

where we have set $D\mathbf{u}^{n+1} := \frac{1}{2}(3\mathbf{u}^{n+1} - 4\mathbf{u}^n + \mathbf{u}^{n-1})$. A pressure correction is computed by solving for ψ^{n+1} and δ^{n+1} in M_h so that the following holds for all $q \in M_h$:

$$\int_{\Omega_{cf}} \nabla \psi^{n+1} \cdot \nabla q = \frac{3}{2\Delta t} \int_{\Omega_{cf}} \mathbf{u}^{n+1} \cdot \nabla q, \tag{3.12}$$

$$\int_{\Omega_{cf}} q \delta^{n+1} = \int_{\Omega_{cf}} q \nabla \cdot \mathbf{u}^{n+1}. \tag{3.13}$$

The pressure is corrected by setting

$$\pi^{n+1} = \pi^n + \psi^{n+1} - R_e^{-1} \delta^{n+1}. \tag{3.14}$$

The above algorithm is exactly the rotational pressure-correction algorithm described in [37] and analyzed in [23]. It may seem unconventional to some readers since the so-called projected velocity has been eliminated as advocated in [20,22].

Once $\mathbf{u}^{n+1}$ is computed we denote by $\tilde{\mathbf{u}}^{n+1}$ the extension of $\mathbf{u}^{n+1}$ to the entire conducting region. Recall that the extension is nonzero if the user wants to model rotating solid parts and zero otherwise. The solution to the Maxwell part of the problem is computed in one step by solving for $\mathbf{H}^{c,n+1}$ in $\mathbf{X}_h^{\mathbf{H}}$ and ϕ^{n+1} in X_h^ϕ so that the following holds for all $\mathbf{b}$ in $\mathbf{X}_h^{\mathbf{H}}$ and all φ in X_h^ϕ:

$$\begin{aligned} &\int_{\Omega_c} \left[\mu^c \frac{D\mathbf{H}^{c,n+1}}{\Delta t} \cdot \mathbf{b} + (R_m \sigma)^{-1} \nabla \times \mathbf{H}^{c,n+1} \cdot \nabla \times \mathbf{b} \right] + \int_{\Omega_c} \mu^\nu \frac{D\phi^{n+1}}{\Delta t} \cdot \nabla \varphi + \int_\Sigma ((R_m \sigma)^{-1} (\nabla \times \mathbf{H}^{c,n+1} - \mathbf{j}^s) - \tilde{\mathbf{u}}^{n+1} \times \mu^c \mathbf{H}^*) \\ &\quad \cdot (\mathbf{b} \times \mathbf{n}^c + \nabla \varphi \times \mathbf{n}^\nu) + g((\mathbf{H}^{c,n+1}, \phi^{n+1}), (\mathbf{b}, \varphi)) + s(\mathbf{H}^{c,n+1}, \mathbf{b}) \\ &= \int_{\Omega_c} (\tilde{\mathbf{u}}^{n+1} \times \mu^c \mathbf{H}^* + (R_m \sigma)^{-1} \mathbf{j}^s) \cdot \nabla \times \mathbf{b} + \int_{\Gamma_c} (\mathbf{a} \times \mathbf{n}) \cdot (\mathbf{b} \times \mathbf{n}) + \int_{\Gamma_\nu} (\mathbf{a} \times \mathbf{n}) \cdot (\nabla \varphi \times \mathbf{n}), \end{aligned} \tag{3.15}$$

where we have set $D\mathbf{H}^{c,n+1} := \frac{1}{2}(3\mathbf{H}^{c,n+1} - 4\mathbf{H}^{c,n} + \mathbf{H}^{c,n-1})$, $D\phi^{n+1} := \frac{1}{2}(3\phi^{n+1} - 4\phi^n + \phi^{n-1})$ and

$$g((\mathbf{H}^{c,n+1}, \phi^{n+1}), (\mathbf{b}, \varphi)) := \beta \sum_{F \in \Sigma_h} h_F^{-1} \int_F (\mathbf{H}^{c,n+1} \times \mathbf{n}^c + \nabla \phi^{n+1} \times \mathbf{n}^\nu) \cdot (\mathbf{b} \times \mathbf{n}^c + \nabla \varphi \times \mathbf{n}^\nu), \tag{3.16}$$

$$s(\mathbf{H}^{c,n+1}, \mathbf{b}) := \gamma \int_{\Omega_c} \nabla \cdot (\mu^c \mathbf{H}^{c,n+1}) \nabla \cdot (\mu^c \mathbf{b}). \tag{3.17}$$

The purpose of the bilinear form g is to penalize the quantity $\mathbf{H}^{c,n+1} \times \mathbf{n}^c + \nabla \phi^{n+1} \times \mathbf{n}^\nu$ across Σ so that it goes to zero when the mesh-size goes to zero. The coefficient β is user-dependent. We usually take $\beta = 1$. The reader is referred to [21] for thorough details and a convergence proof.

The purpose of the bilinear form s is to have a control on the divergence of $\mu^c \mathbf{H}^c$, although this control is not really necessary. Adding the bilinear form s amounts to replacing the Faraday equation by the following equivalent PDE's:

$$\mu^c \partial_t \mathbf{H}^c = -\nabla \times \mathbf{E}^c + \mu^c \nabla(\gamma \nabla \cdot (\mu^c \mathbf{H}^c)), \tag{3.18}$$

$$\nabla \cdot (\mu^c \mathbf{H}^c)|_{\partial\Omega_c} = 0. \tag{3.19}$$

Depending of the regularity of Σ we either take $\gamma = 1$ or $\gamma = 0$. We set $\gamma = 1$ when Σ is smooth or piecewise smooth and has no re-entrant corner, otherwise we set $\gamma = 0$. It is known that when using Lagrange elements and when Σ has re-entrant corners using the stabilizing bilinear form s leads to convergence loss, i.e., it may happen that a singular component of the solution is not computed if the interface is not smooth (see Costabel's Lemma [13]). Based on ideas from [9], we are currently developing a stabilization technique that avoids this possible inconvenience.

Due to the fact that the nonlinear terms are made explicit using the so-called Adams–Bashforth extrapolation (3.10), the above scheme is stable under a CFL condition. In practice the CFL number is of order one or smaller. Measured in the L^2-norm, the scheme is formally second-order in time for all variables, third-order in space for the velocity, second-order in space for the pressure, second and a half-order in space for the magnetic and potential fields.

3.6. Linear systems

It is clear that at each time step the algorithm (3.10)–(3.17) leads to as many independent linear systems as Fourier modes. For instance, let n_p and $n_{\mathbf{u}}$ be the number of $\mathbb{P}_1$ and $\mathbb{P}_2$ nodes in the two-dimensional mesh $\mathcal{F}_h^{cf}$, i.e., $\dim(M_h^{2D}) = 2n_p$ and $\dim(\mathbf{V}_h^{2D}) = 6n_{\mathbf{u}}$. Then, for each Fourier mode (3.11) gives two linear systems of size $2n_{\mathbf{u}}$ (the r- and θ-components of the velocity field are coupled) and two linear systems of size $n_{\mathbf{u}}$ (the z-component of the velocity field is uncoupled). Problems (3.12) and (3.13) each give two systems of size n_p. Let $n_{\mathbf{H}}$ be the number of $\mathbb{P}_1$ nodes in the two-dimensional mesh $\mathcal{F}_h^c$ if $\ell_{\mathbf{H}} = 1$ or number of $\mathbb{P}_2$ nodes if $\ell_{\mathbf{H}} = 2$ and let n_ϕ be the number of $\mathbb{P}_1$ nodes in the mesh $\mathcal{F}_h^v$ if $\ell_\phi = 1$ or $\mathbb{P}_2$ nodes if $\ell_\phi = 2$. For each Fourier mode, (3.15) gives two linear systems of size $3n_{\mathbf{H}} + n_\phi$; see Table 1.

The linear systems are solved using a preconditioned biCG-stab algorithm, the preconditioner being the incomplete LU factorization with thresholding (ILUT). The maximum of nonzero entries for each line in each ILUT factorization is set to 70. The band-width of each preconditioner is minimized by re-ordering the degrees of freedom using a Cuthill/McKee-like method (see e.g. [30,16]). The linear systems are considered to be solved when the residual is reduced by a 10^{-6} ratio. Two to twenty biCG-stab iterations are needed depending on the problem to be solved. We observed that the complexity of our preconditioned biCG-stab algorithm is $\mathcal{O}(N^{1.25})$ for a Laplace-like equation, where N is the number of degrees of freedom.

If there were no nonlinear terms, the above linear systems associated with each Fourier mode could be solved in parallel. In principle we could use as many processors as Fourier modes. Of course, this picture is idealistic since all the modes are coupled through the nonlinear terms. Nevertheless, this is the model we have chosen to parallelize the code. Given a number of Fourier modes, say $M+1$, we perform the computation on N_{proc} processors so that N_{proc} divides $M+1$. Then, the modes are divided into blocs of size $N_b := (M+1)/N_{\text{proc}}$ and each bloc of Fourier modes is assigned to one processor. If $M+1$ processors are available, one simple choice is to take $N_{\text{proc}} = M+1$.

3.7. Computation of nonlinear terms

The nonlinear terms are computed using a pseudo-spectral method without de-aliasing and the fast Fourier transform subroutines from the FFTW3 package [17]. In the rest of this section we describe how we have implemented FFTW3 so as to reduce communication times. All the nonlinear terms are of the form $\mathbf{A} \times \mathbf{B}$ and must be computed either at the Gauss points or at the nodes of the mesh of the meridian section (using Gauss points is more accurate but slightly more expensive since there are more Gauss points than nodes). In practice, the vectors $\mathbf{A}$ and $\mathbf{B}$ are the three-dimensional vector fields $\mathbf{u}$, $\mathbf{H}$, $\nabla \times \mathbf{u}$, or $\nabla \times \mathbf{H}$.

Let n_g be the number of nodes or Gauss points in the meridian plane where the cross products have to be evaluated; these points are labeled $1, \dots, n_g$. Denote by $\widehat{\mathbf{A}}$ and $\widehat{\mathbf{B}}$ the collection of the associated Fourier modes at the n_g points. The Fourier nodes are labeled $0, \dots, M$. If needed, artificial data are added to $\widehat{\mathbf{A}}$ and $\widehat{\mathbf{B}}$ so that n_g is a multiple of N_{proc}. Assume that the collection of Fourier modes $\widehat{\mathbf{A}}$ has been distributed so that processor P_i, $0 \leqslant i \leqslant N_{\text{proc}} - 1$, takes care of the modes of indices $iN_b, \dots, (i+1)N_b - 1$ of the n_g points. We denote by $\widehat{\mathbf{A}}_i$ the bloc of data assigned to processor P_i; these are $3 \times N_b \times n_g$ complex numbers. We further divide $\widehat{\mathbf{A}}_i$ into N_{proc} blocs so that bloc j, $0 \leqslant j \leqslant N_{\text{proc}} - 1$, contains the Fourier coefficients of the points of indices $jn_g/N_{\text{proc}} + 1, \dots, (j+1)n_g/N_{\text{proc}}$; the bloc in question is denoted by $\widehat{\mathbf{A}}_{i,j}$. As a result bloc $\widehat{\mathbf{A}}_{i,j}$ contains $3 \times ((M+1)/N_{\text{proc}}) \times (n_g/N_{\text{proc}})$ complex numbers. Using the MPI protocol, the bloc matrices $(\widehat{\mathbf{A}}_{i,j})$ and $(\widehat{\mathbf{B}}_{i,j})$, $0 \leqslant i,j \leqslant N_{\text{proc}} - 1$ are transposed by one call to the MPI_ALLTOALL subroutine. After this call the processor P_i has access to the blocs $\widehat{\mathbf{A}}_{0,i}, \dots, \widehat{\mathbf{A}}_{N_{\text{proc}}-1,i}$, i.e., these are all the Fourier modes of the points of indices $in_g/N_{\text{proc}} + 1, \dots, (i+1)n_g/N_{\text{proc}}$. The real values associated with these Fourier modes are evaluated at the angles $0, \dots, \frac{2k\pi}{2M+1}, \dots, \frac{2M\pi}{2M+1}$, using the complex to

Table 1
Summary of linear operations.

Eq.	Fields	Size of lin. syst.	# of lin. syst.
(3.11)	u_r, u_θ	$2\,n_{\mathbf{u}}$	2
(3.11)	u_z	$n_{\mathbf{u}}$	2
(3.12)	$\pi := p + \frac{1}{2}\mathbf{u}^2$	n_p	2
(3.13)	δ	n_p	2
(3.15)	$\mathbf{H}$, ϕ	$3n_{\mathbf{H}} + n_\phi$	2

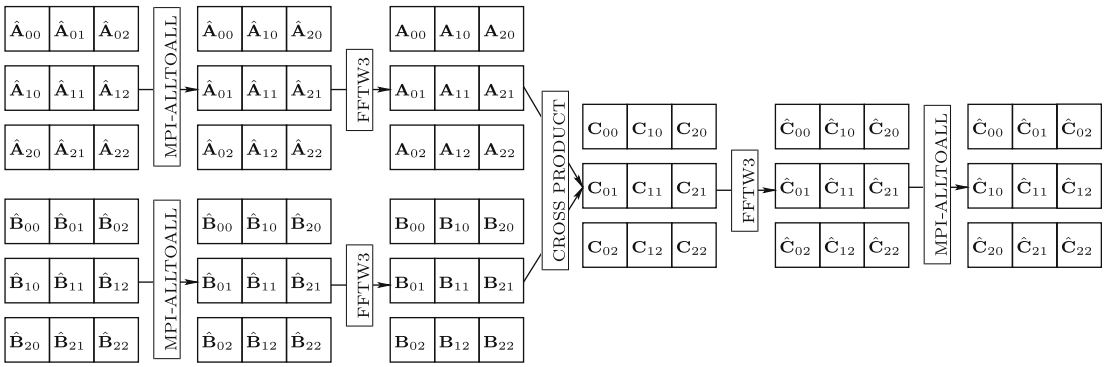

Fig. 2. Use of MPI_ALLTOALL and FFTW3.

real FFTW3 subroutine; the cross products are then evaluated and stored in blocs $\mathbf{C}_{0,i},\ldots,\mathbf{C}_{N_{\text{proc}}-1,i}$. The corresponding Fourier coefficients are then computed by using the real to complex FFTW3 subroutine and stored in the bloc structure $\widehat{\mathbf{C}}_{0,i},\ldots,\widehat{\mathbf{C}}_{N_{\text{proc}}-1,i}$. The Fourier modes are finally redistributed among the processors, i.e., the bloc matrix is transposed by calling again the MPI_ALLTOALL subroutine. The entire procedure is schematically described in Fig. 2.

Communications are restricted to the two calls to the MPI_ALLTOALL subroutine. At each communication cycle each processor sends and receives $3\times N_b\times n_g\times(N_{\text{proc}}-1)/N_{\text{proc}}$ complex numbers. The main feature of this protocol is that the number of data exchanged on each processor is of the same order as the number of points in the meridian plane, n_g.

3.8. Parallelization tests

We have made two series of tests to assess the parallelization performance of the code. In the first series we have tested the subroutine performing the pseudo-spectral evaluation of cross products and in a second test we have evaluated the Navier–Stokes part of the code. The first test assesses the impact of communication whereas the second assesses the load balancing. The tests have been performed on an IBM SP4 cluster of processors of IDRIS.

Since computing the cross products is the only part in the code that requires communication, we have spent some time trying to optimize it. We report in Tables 2 and 3 the results of two tests done with two different sets of parameters M and n_g. Efficiency coefficients larger than one are probably due to memory cache effects. As the number of processors increases, each processor treats smaller sets of data which better fit in the fast internal memory. Recalling that $(2M+1)*n_g$ represents the number of nodes in the corresponding three-dimensional mesh, these two tests approximately correspond to 6×10^6 grid points. Despite the relatively large amount of inter-processor communication involved in the algorithm (see Fig. 2) we observe extremely good scaling with the number of processors in the two test cases. This is due to the fact that the IBM SP4 architecture has very fast connections between nodes. These somewhat surprising observations are similar to those made in [7, Section 2.6].

In the second test we have solved the Navier–Stokes equations using $M+1=16$ complex Fourier modes in a cylinder whose meridian rectangular section is discretized using 46,985 $\mathbb{P}_2$ nodes. The three-dimensional mesh is then composed of approximately 1.5×10^6 velocity degrees of freedoms. At low Reynolds numbers, i.e., when the nonlinear terms are not really active, the parallel efficiency goes down to less than 50%. This is due to the fact that the processors in charge of the higher Fourier modes have a smaller load; they still participate to the computation of the cross products through the FFTs, but the time spent for solving the linear systems is negligible since, the Fourier coefficients being close to zero, it is easy to

Table 2
FFT test using $M+1=64$, $n_g=50,000$.

# processors	1	2	4	8	16	32	64
Speed up	1.000	2.092	4.016	9.648	18.72	32.94	54.50
Efficiency	1.000	1.046	1.004	1.206	1.170	1.029	0.852

Table 3
FFT test using $M+1=30$, $n_g=100,000$.

# processors	1	2	6	10	15	30
Speed up	1.000	2.098	5.347	11.48	17.62	32.53
Efficiency	1.000	1.049	0.891	1.148	1.175	1.084

Table 4
Navier–Stokes test, $M+1=16$, $n_g=46,985$.

# processors	1	2	4	8	16
Speed up	1.000	1.549	4.032	5.751	14.45
Efficiency	1.000	0.775	1.008	0.719	0.903

make a very accurate initial guess of the solution. When the Reynolds number is large enough so that all the Fourier modes are populated, we recover parallel efficiency coefficients close to one. Table 4 shows the results of one typical test.

This test shows that load balancing issues may occur when the Fourier modes are equally distributed among the processors and some of these modes are inactive or have low activity. There is no issue though when all the Fourier modes are active.

4. Periodic and finite Taylor–Couette dynamos

The Taylor–Couette flow is one of the most intensively studied flows using either analytical, experimental, or numerical tools (see [34] and references therein). The MHD version of this problem is largely unexplored due to the difficulty of dealing with magnetic boundary conditions in bounded domains. The purpose of this section is twofold. First we validate our code by making comparisons with published results on z-periodic solutions [38] proving that the Taylor–Couette flow of conducting fluid can sustain dynamo action. Second, we consider a finite setting, i.e., non-periodic in the axial direction and we uncover a new type of cyclic nonlinear dynamo. Comparisons between the periodic and finite cases are discussed. In this entire section μ is constant and $\mu^c=\mu^v$.

4.1. The physical setting

We consider an incompressible fluid, of kinematic viscosity ν, contained between two coaxial cylinders of height or axial period L_z. The radius of the inner cylinder is R_i and that of the outer one is R_o. The inner cylinder rotates with angular velocity Ω_i and the outer one is static. The magnetic permeability is assumed to be constant, say μ_0. The conductivity is also assumed to be constant, say σ_0.

We use $\mathcal{L}=R_o-R_i$ as unit length, $\mathcal{U}=\Omega_i R_i$ as unit velocity and $\mathcal{H}=\mathcal{U}\sqrt{\rho/\mu_0}$ as unit magnetic field. The governing non-dimensional parameters of the system are the kinetic Reynolds number, R_e, the magnetic Reynolds number, R_m, the radius ratio η and the aspect ratio Γ,

$$R_e=\frac{\mathcal{U}\mathcal{L}}{\nu},\quad R_m=\mu_0\sigma_0\mathcal{U}\mathcal{L},\quad \eta=\frac{R_i}{R_o},\quad \Gamma=\frac{L_z}{\mathcal{L}}. \tag{4.1}$$

Whenever the context makes confusion impossible, we abuse the notation by using the same letters for dimensional and non-dimensional quantities. In the following, we set $\eta=0.5$. This immediately implies, $R_i=1$, $R_o=2$, $\Omega_i=1$. Therefore, the conducting domain Ω_c containing the fluid is defined in cylindrical coordinates by $r\in[1,2]$, $\theta\in[0,2\pi]$ and $z\in[-\Gamma/2,\Gamma/2]$. Two situations are considered and compared. In the first case we assume that the problem is periodic in the z-direction and we set $\Gamma=4$. In the second case we assume that the vertical extension of the cylinders is finite and we set $\Gamma=2\pi$. In both cases the two cylinders are surrounded by vacuum and the vacuum domain is truncated for numerical purposes. In the first case (i.e., periodicity in z-direction), the vacuum region of height Γ extends from $r=0$ to $r=1$ and from $r=2$ to $r=10$. In the second case (i.e., finite vertical extension) the vacuum region is bounded by a sphere of radius $R_s=10$. We have verified that truncating the vacuum domain to a sphere or cylinder with a radius 10 times larger than the reference length scale is sufficient to guarantee less than one per cent accuracy due to truncation.

4.2. Numerical details

The velocity and magnetic fields in Ω_c are approximated using $\mathbb{P}_2$ Lagrange polynomials and the pressure field is approximated using $\mathbb{P}_1$ polynomials. In the vacuum Ω_v, the magnetic potential ϕ is approximated using $\mathbb{P}_2$ Lagrange polynomials. Typical characteristics of all the cases studied in Sections 4.3–4.5 are summarized in Table 5.

Table 5
Characteristics of the runs: h is the uniform or non-uniform mesh-size in Ω_c; Δt is the timestep; $np(P)$ is the number of $\mathbb{P}_1$ nodes for the pressure field in Ω_c; $np(H)$ is the number of $\mathbb{P}_2$ nodes for the magnetic and velocity fields in Ω_c; $np(\phi)$ is the number of $\mathbb{P}_2$ nodes for the magnetic potential in Ω_v.

Boundary cond.	h	Δt	$np(P)$	$np(H)$	$np(\phi)$
Finite	1/80	0.025	11,893	46,985	31,870
z-Periodic	1/100–1/25	0.025	3603	14,113	16,424

We have done all the computations on four different meshes, $h = 1/20$, $h = 1/40$, $h = 1/80$, $h = 1/100$. We have verified that all the results are comparable within a 3% range when $h \leqslant 1/40$. The computations reported below are done using $h = 1/80$. In all the computations reported below, the relative L^2-norm of the divergence of the velocity and the magnetic induction are of order 2.4×10^{-2} and 4.0×10^{-4}, respectively.

Illustrations of the finite element meshes of the conducting and non-conducting regions are shown in Fig. 3; the mesh-sizes have been coarsened for visualization purposes.

The computations have been performed on the IBM SP4 machine of IDRIS. The Navier–Stokes computations reported in Section 4.3 require 10^{-5} CPU seconds per degree of freedom and per time step. The Maxwell computations reported in Section 4.4 require 2.6×10^{-5} CPU seconds per degree of freedom and per time step per processor. The nonlinear MHD computations reported in Section 4.5 require 3.8×10^{-5} CPU seconds per degree of freedom and per time step per processor.

4.3. First hydrodynamic bifurcation

In this section, the Navier–Stokes equations are solved in the absence of magnetic field. At low Reynolds numbers the fluid flow is axisymmetric and is purely azimuthal in the periodic case (i.e., the Couette flow). As R_e increases and goes beyond a critical value R_{ec}, the flow becomes centrifugally unstable to axisymmetric rolls (Taylor vortices) which break the translational symmetry along the axis of the cylinders. The purpose of this section is to describe this bifurcation as a validation of the Navier–Stokes code.

4.3.1. z-Periodic case

Taylor [35] computed the threshold of the first hydrodynamic bifurcation by neglecting the effects of the top and bottom plates of the experiment and therefore assuming that the vortices are periodic along the axis. With $\eta = 0.5$, the critical Reynolds number of the first bifurcation is $R_{ec}^{Ch} = 68.23$ for the aspect ratio $\Gamma^{Ch} = 1.96$ [11] corresponding to a pair of counter-rotating rolls of approximately unit aspect ratio in (r, z). In our computation, we set $\Gamma = 4$, like in [38], so as to have room for two pairs of Taylor vortices and one magnetic structure (see below). The computation is done using the $m = 0$ azimuthal Fourier mode only. We assume periodic boundary conditions for $\mathbf{u}$ at $z = \pm\Gamma/2$. The other boundary conditions are

$$\mathbf{u}(r = 1, z) = \mathbf{e}_\theta, \quad \mathbf{u}(r = 2, z) = 0. \tag{4.2}$$

The bifurcation connecting the circular Couette basic state [35] to the Taylor vortices is of supercritical pitchfork type. The strength of the transition between the two states, measured by the strength of the rolls (for example the radial velocity

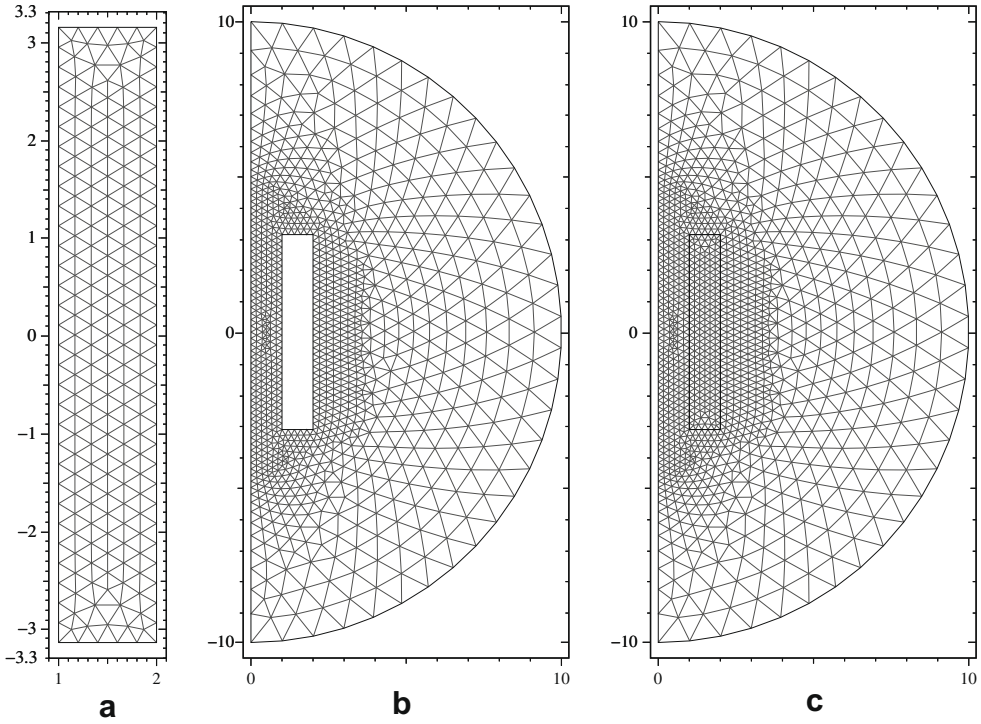

Fig. 3. Illustrations of the finite element meshes of the conducting (a) and non-conducting (b) regions.

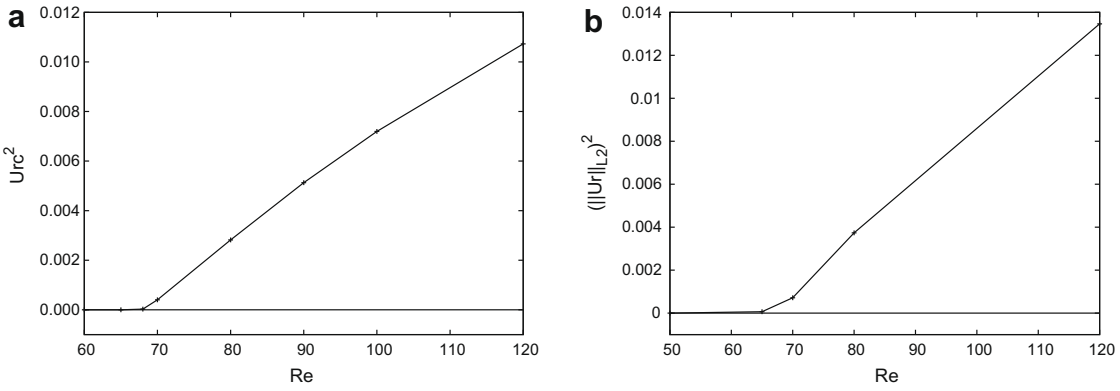

Fig. 4. Bifurcation diagram for Taylor–Couette flow. (a) Squared radial velocity component at $(z = 0, r = 1.7)$ as a function of R_e for the periodic case with $\Gamma = 4$. (b) Squared L^2 norm of the radial velocity component computed in a small equatorial region $(1 \leqslant r \leqslant 2, -0.01 \leqslant z \leqslant 0.01)$ as a function of R_e for the finite case with $\Gamma = 2\pi$.

component at $z = 0, r = 1.7$ in Fig. 4(a), varies as the square root of $R_e - R_{ec}$. Our computations give $R_{ec}^{perio} \approx 68$, which is close to the quoted value $R_{ec}^{Ch} = 68.23$. The velocity field is shown in Fig. 5(a) and (b) for a subcritical (Couette flow) and a supercritical Reynolds number (Taylor vortex flow). The nonlinear Taylor vortex flow thus obtained, hereafter denoted by $\mathbf{V}_{VF}^{perio}$, is used for kinematic dynamo computations which are reported in Section 4.4. With the above parameter values, the second transition to wavy vortices occurs at a larger Reynolds number, $R_e > 272$ [24].

4.3.2. Finite case

We now assume no-slip boundary conditions for $\mathbf{u}$ at $z = \pm\Gamma/2$. The top and bottom plates break the translational symmetry along the cylinder axis. Experimentalists have studied settings with large values of Γ in order to mimic the periodic case [35,3]. Experiments conducted with small values for Γ, say $\Gamma \approx O(1)$, have detected anomalous bifurcation branches [5,12]. The small aspect ratio region has also been investigated with the help of numerical simulations [27,26] and is known to exhibit complicated dynamics where the rotation symmetry about the cylinder axis and the equatorial symmetry about the $z = 0$ plane play crucial roles. Since we do not want to mix the dynamo and the hydrodynamic symmetry features, we choose an intermediate value of the cylinder aspect ratio, $\Gamma = 2\pi$. Again, the computations are done using the $m = 0$ azimuthal Fourier mode only. The boundary conditions are now as follows:

$$\mathbf{u}(r = 1, z) = \mathbf{e}_\theta, \quad \mathbf{u}(r = 2, z) = 0, \quad \mathbf{u}(r, z = \pm\pi) = 0. \tag{4.3}$$

Bödewadt boundary layers at the top and bottom static plates cause the fluid to spiral inwards for any R_e. Taylor vortices of small amplitude develop in the boundary layers (see Fig. 5(c)) and invade the bulk of the system as R_e approaches R_{ec} (see Fig. 5(d)) [1,29].

Benjamin [3,4] interpreted the formation of Taylor vortices in a finite experiment as an imperfect pitchfork bifurcation (see Fig. 4(b)). We compute the bifurcation threshold by linearly interpolating the square of the L^2-norm of the radial velocity, the L^2-norm being computed in a small region around the equatorial plane. We obtain $R_{ec}^{finite} \approx 65$, to be compared to $R_{ec}^{perio} \approx 68$. For $R_e = 120$, Fig. 5(d) shows three pairs of steady counter-rotating meridional vortices of almost square shape. Three wavelengths fit in the domain. This flow has the following symmetry properties with respect to the equatorial plane $z = 0$: $(U_r, U_\theta, U_z)(r, \theta, -z) = (U_r, U_\theta, -U_z)(r, \theta, z)$ that we refer to as the symmetric state. The nonlinear Taylor vortex flow thus obtained is henceforth denoted by $\mathbf{V}_{VF}^{finite}$ and is used for kinematic dynamo computations which are reported in the next section.

Since the ratio of poloidal (meridional) to toroidal (azimuthal) velocity is an important flow parameter for kinematic dynamo computations we report in Table 6 the maximum of the various components at $R_e = 120$ for $\mathbf{V}_{VF}^{perio}$ and $\mathbf{V}_{VF}^{finite}$. It is known that in the periodical case the poloidal to toroidal ratio ≈ 0.15 yields dynamo action, see [38]. From Table 6, we observe that this ratio is again ≈ 0.15 in the finite case, we then expect to obtain the dynamo action in the finite setting also (this is confirmed in Sections 4.4 and 4.5.2).

4.4. Kinematic dynamo

We use the nonlinear Taylor vortex flow $\mathbf{V}_{VF}^{perio}$ or $\mathbf{V}_{VF}^{finite}$ obtained at $R_e = 120$ to solve the induction equation (kinematic regime). Since both flows are axisymmetric, the term $\nabla \times (\mathbf{V}_{VF} \times \mathbf{H}^c)$ cannot transfer energy between the azimuthal modes of $\mathbf{H}^c$, i.e., the azimuthal modes are uncoupled. The first bifurcation is of Hopf type and the unstable eigenvector corresponds to the Fourier mode $m = 1$ [25,38]; consequently, we set the initial small magnetic seed field in the conductor to be

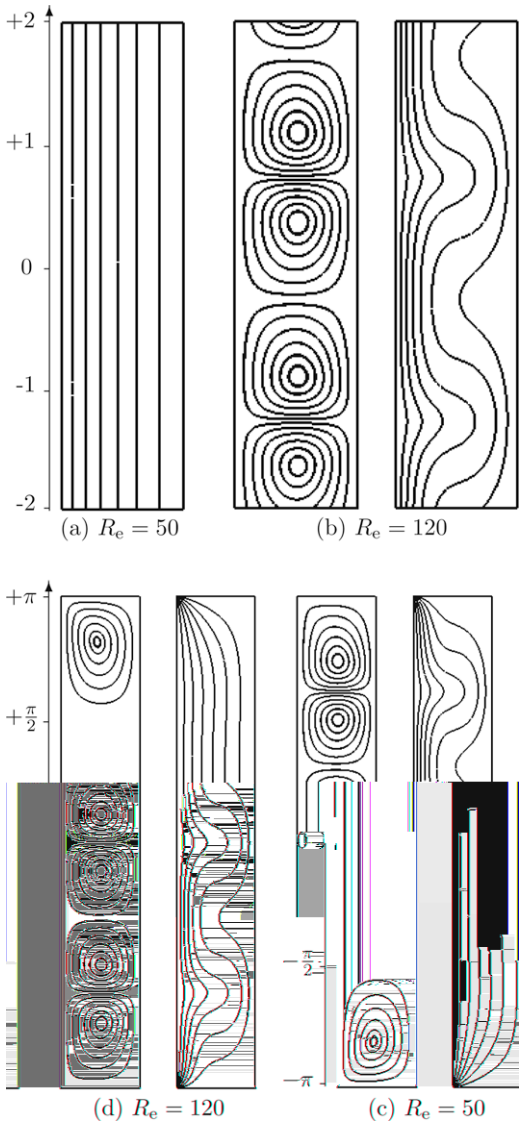

Fig. 5. Taylor–Couette flow with $\Gamma = 4$ ($\mathbf{V}_{VF}^{perio}$, a–b) and $\Gamma = 2\pi$ ($\mathbf{V}_{VF}^{finite}$, c–d) at $R_e = 50$ (left) and $R_e = 120$ (right). Represented are the meridional velocity field streamlines and the azimuthal component.

$$\begin{cases} H_r = \frac{1}{r} f(r)\cos(\theta)\sin(k_0 z), \\ H_\theta = -f'(r)\sin(\theta)\sin(k_0 z), \\ H_z = 0 \end{cases} \tag{4.4}$$

with $k_0 = n_0 2\pi/\Gamma$, $n_0 \in \mathbb{N}$ being a parameter and $f(r) = A(R_i - r)^2(R_o - r)^2$. This magnetic field is compatible with $\phi_0 = 0$ in the vacuum.

The magnetic energy of the $m = 1$ mode, $\frac{1}{2}\int_{\Omega_c^{2D}} \|\mathbf{H}^c(m=1)\|^2 d\mathbf{x}$, is recorded as a function of time for various magnetic Reynolds numbers $R_m \in [150, 480]$; the notation $\mathbf{H}^c(m=1)$ refers to the Fourier mode $m = 1$ of $\mathbf{H}^c$. The growth rate of the

Table 6
Maxima of $\mathbf{V}_{VF}^{perio}$ and $\mathbf{V}_{VF}^{finite}$ at $R_e = 120$.

$R_e = 120$	Perio $\Gamma = 4$	Finite $\Gamma = 2\pi$
max u_r	0.1935	0.1967
max u_θ	1	1
max u_z	0.1454	0.1564

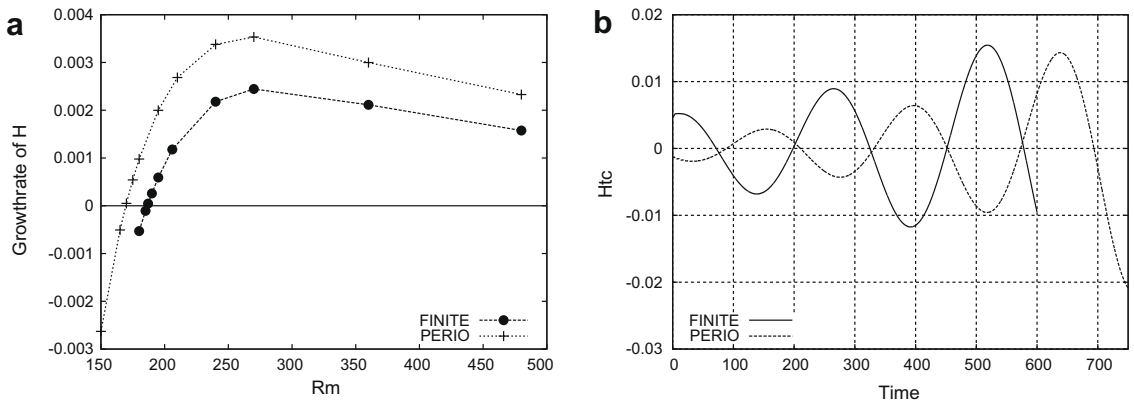

Fig. 6. Kinematic dynamo. (a) Growth rate of the magnetic field for Taylor–Couette flow with $\Gamma = 4$ (periodic) or $\Gamma = 2\pi$ (finite) at $R_e = 120$ as a function of R_m. (b) Time evolution of the azimuthal component of the magnetic field at $(r = 1.2, z = -1)$ for both cases at $R_e = 120$ and $R_m = 240$.

magnetic field (i.e., the real part of the leading eigenvalue) is reported in Fig. 6(a) for the two configurations considered (finite and periodic domains). We have verified that different initial conditions with wavenumbers $n_0 = 1$ or $n_0 = 2$ lead to the same asymptotic time evolution. The two critical magnetic Reynolds numbers, defined so that the growth rate of the magnetic field is zero, are $R_{mc}^{perio} = 170 \pm 1$ and $R_{mc}^{finite} = 187 \pm 1$ at $R_e = 120$. The difference between these two thresholds can be explained by the differences in the topology of the velocity fields. The top and bottom vortices induced by the Bödewadt boundary layers in the finite case are impediments to the growth of the magnetic field and, as a result, delay the bifurcation.

When R_m is larger than the critical value, recordings of the time evolution of the magnetic field at various points in the fluid domain show that the signal is the product of a growing exponential and a time-periodic component. We observe that the period of the oscillating component is $T^{finite} \approx 252$ and $T^{perio} \approx 242$ for $R_e = 120$ and $R_m = 240$ (see Fig. 6(b)). The dominant component of the magnetic field is the azimuthal one, the radial and vertical components being smaller and of the same order.

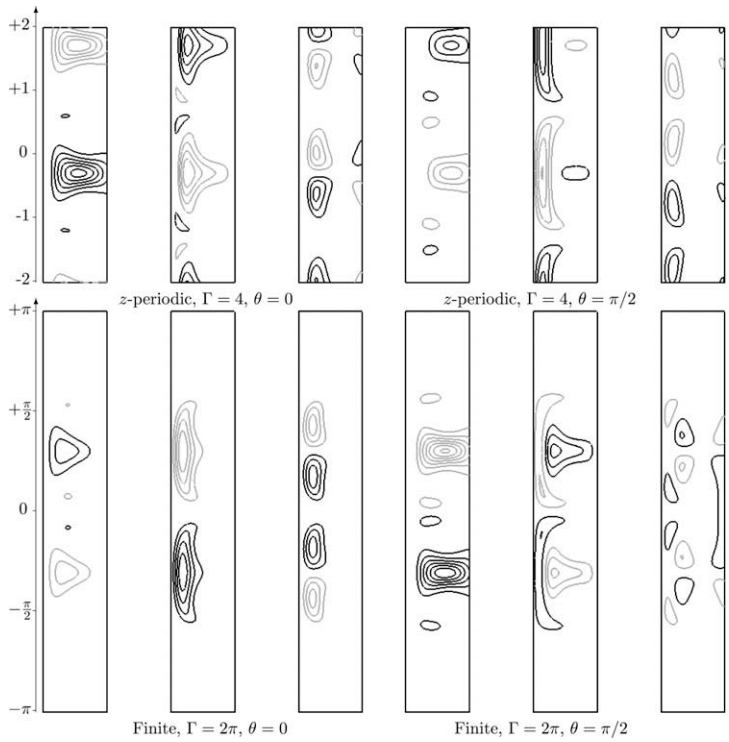

Fig. 7. Kinematic dynamo. Magnetic eigenvector (H_r, H_θ, H_z) at $R_e = 120$ and $R_m = 240$. Represented are the radial (16 levels between $-0.4 \leqslant H_r \leqslant 0.4$), azimuthal (10 levels between $-1 \leqslant H_\theta \leqslant 1$) and vertical (6 levels between $-0.15 \leqslant H_z \leqslant 0.15$) components normalized by the maximum of the azimuthal component.

Iso-lines of the three components of magnetic eigenvectors are shown in Fig. 7 at planes $\theta = 0$ and $\theta = \pi/2$ for the periodic and finite cases. Iso-surfaces of the modulus of the magnetic eigenvectors are shown in Fig. 8. In both cases, the eigenfunction has a $m = 1$ symmetry. Note that, as expected [25], the magnetic wavelength is about twice that of the velocity in both cases; there is no scale separation in this kinematic dynamo. Both magnetic eigenvectors show similar features. In the finite case, this magnetic structure has the following symmetry properties with respect to the equatorial plane $z = 0$: $(H_r, H_\theta, H_z)(r, \theta, -z, t) = (-H_r, -H_\theta, H_z)(r, \theta, z, t)$ that we refer to as the antisymmetric magnetic state (also sometimes named 'dipole' solution in the astrophysical literature). The same symmetry properties hold in the periodic case with respect to planes $z = 0.7$ and $z = -1.3$. Note that, at the symmetry planes, $z = 0$ (finite case) or $z = 0.7$ and $z = -1.3$ (periodic case), $H_r = 0 = H_\theta$ and $H_z \neq 0$. The two magnetic blobs constituting the magnetic structure are connected via these nonzero H_z zones (see Fig. 8(a) and (b)) in both cases. However, in the finite case, due to the value of the finite height, only one magnetic pair can fit in the domain.

4.5. Nonlinear dynamo

In this section, we perform nonlinear dynamo computations at $R_e = 120$ and $R_m = 240$. We work with 12 azimuthal modes ($m = 0, \ldots, 11$) and the meridional finite element mesh is the same as that used in the kinematic runs. The initial velocity field is the axisymmetric Taylor vortex flow $\mathbf{V}_{VF}^{perio}$ or $\mathbf{V}_{VF}^{finite}$ for $R_e = 120$ and the initial magnetic seed is the growing mode obtained in the kinematic computations (Section 4.4, $R_m = 240$).

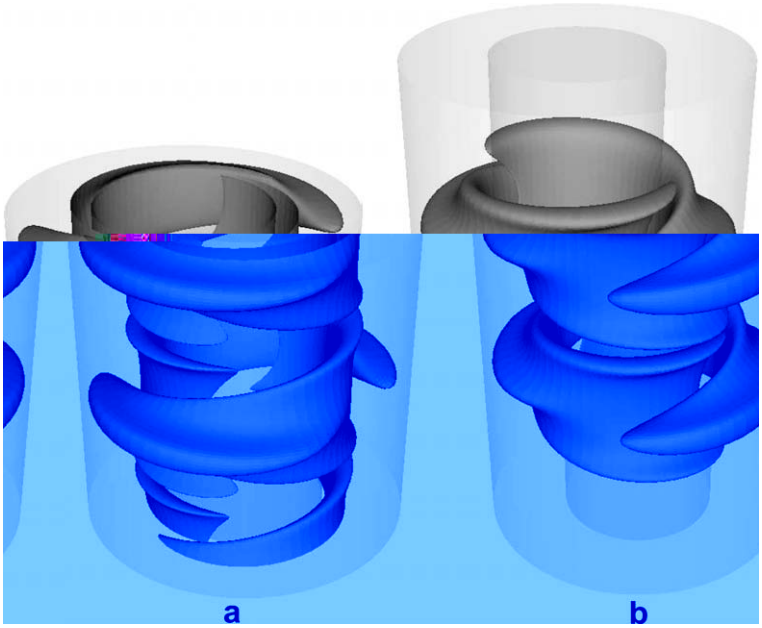

Fig. 8. Kinematic dynamo. Isosurface of $|\mathbf{H}|$ at $R_e = 120$ and $R_m = 240$ for (a) the periodic case and (b) the finite case (25% of maximum values).

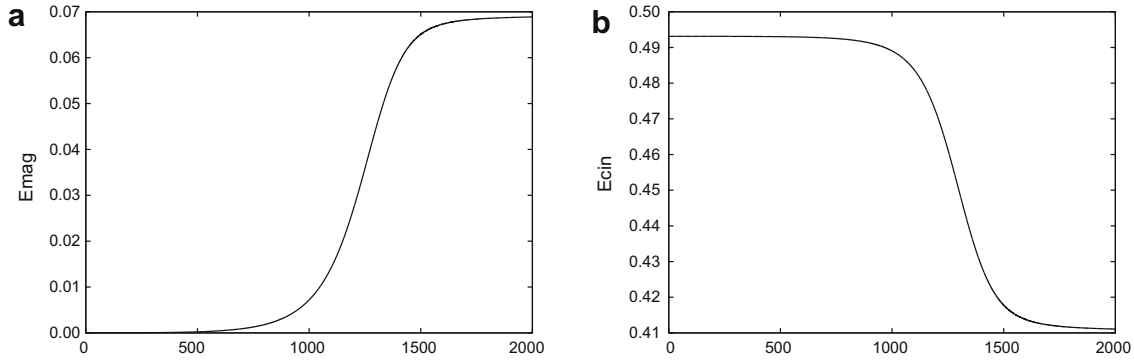

Fig. 9. Nonlinear dynamo in the z-periodic case. Time evolution of (a) magnetic and (b) kinetic energies in the conducting region $R_i \leqslant r \leqslant R_o$ and $-\Gamma/2 \leqslant z \leqslant \Gamma/2$.

4.5.1. z-Periodic case

The time evolution of the kinetic and magnetic energies in the periodic configuration is reported in Fig. 9. The kinetic and magnetic energies are defined as follows, $\frac{1}{2}\int_{\Omega_c}\|\mathbf{u}\|^2 d\mathbf{x}$, $\frac{1}{2}\int_{\Omega_c}\|\mathbf{H}^c\|^2 d\mathbf{x}$, respectively. As in [38], the magnetic energy first increases exponentially and then saturates. Contrary to the kinematic case, the flow is modified by the Lorentz force: the braking action (Lenz rule) is directly visible on the evolution of the total kinetic energy which experiences a decrease of about 16%. The final nonlinear MHD state is a steady rotating wave and results from the balance between the driving effect of the viscous shear and the braking effect of the Lorentz force.

In the nonlinear regime, the fluid flow loses the $m = 0$ symmetry and the magnetic field loses the $m = 1$ symmetry. The flow is forced by the Lorentz force $(\nabla \times \mathbf{H}) \times \mathbf{H}$ and acquires a $m = 2$ contribution. The magnetic field is deformed by the action of the induction term and acquires a $m = 3$ perturbation. By consequence, the coupling terms generate even azimuthal velocity modes, $m = 0, 2, \ldots$ and odd azimuthal magnetic modes, $m = 1, 3, \ldots$ At saturation the velocity mode $m = 0$ is dominant. We show in Fig. 10(a) and in the subsequent figures the velocity structure without the $m = 0$ contribution so as to better distinguish the fine structures. The modulus of the magnetic field at saturation is shown in Fig. 10(b). The symmetry properties of the kinematic case are conserved in the nonlinear regime.

4.5.2. Finite case

To our knowledge, the numerical study of this MHD configuration is new. In contrast with the steady dynamo in the z-periodic case, we obtain a cyclic dynamo regime when the z-extension of the fluid domain is finite.

Fig. 11 shows the time evolution of the kinetic and magnetic energies for the aspect ratio $\Gamma = 2\pi$. From $t = 0$ to $t = 800$ (first phase), the kinetic energy decreases and the magnetic energy grows exponentially with a growth rate similar to that of the kinematic dynamo. Then, in the nonlinear regime, both the magnetic and the kinetic energies seem to saturate, but at $t = 1200$ the magnetic energy starts to decrease and the kinetic energy starts to increase (for $1200 \leqslant t \leqslant 2250$). The system

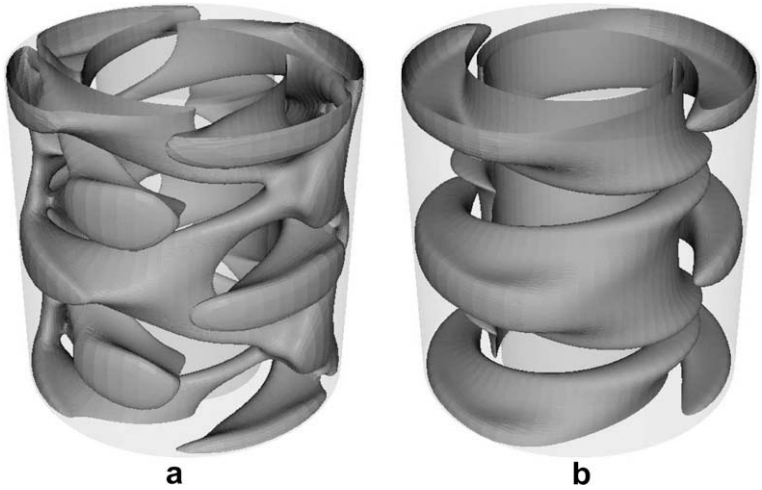

Fig. 10. Periodic nonlinear dynamo at saturation, $R_e = 120$, $R_m = 240$. Isosurface of (a) $|\mathbf{u}|$ without $m = 0$ contribution and (b) $|\mathbf{H}|$ (25% of maximum values).

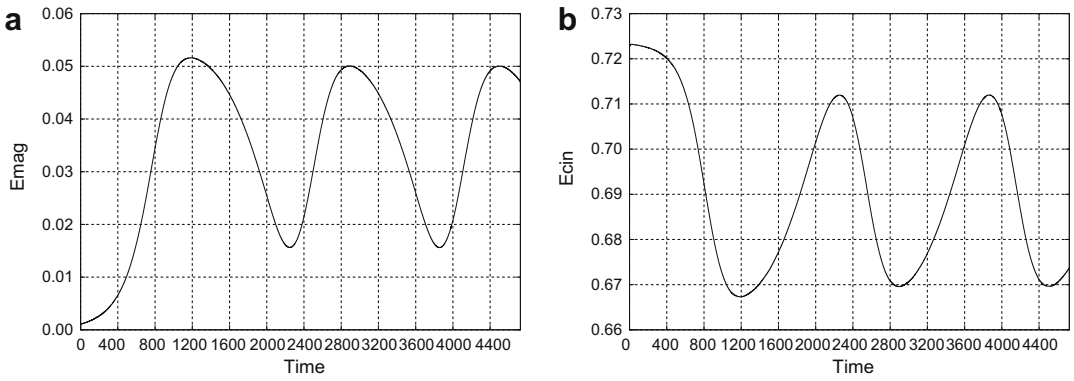

Fig. 11. Nonlinear dynamo in the finite case. Time evolution of (a) magnetic and (b) kinetic energies in the conducting region $R_i \leqslant r \leqslant R_o$ and $-\Gamma/2 \leqslant z \leqslant \Gamma/2$.

enters a cyclic regime. The magnetic energy reaches a minimum at $t \approx 2250$ followed by a maximum at $t \approx 2900$, a minimum at $t \approx 3850$ and a maximum at $t \approx 4500$. The first arch (for $0 \leqslant t \leqslant 2250$) corresponds to a long transitory regime which is followed by two cycles of about 1600 time units, where magnetic and kinetic energies oscillate in opposition.

The main new feature during the time evolution is the breaking of the equatorial symmetry of the solution. The non-magnetic flow at $R_e = 120$ has a planar symmetry both in the z-periodic and finite cases, see Fig. 5 (the azimuthal velocity is even with respect to z). In the case of the kinematic dynamo ($R_m = 240$) the magnetic field is antisymmetric with respect to z (dipole-like) both in the z-periodic and finite cases, see Fig. 7. We show in Fig. 12 the azimuthal velocity and magnetic fields in the MHD regime (without the axisymmetric component) at five typical times $t_a = 800$, $t_b = 1200$, $t_c = 1900$, $t_d = 2300$, $t_e = 2500$, for the finite case. Table 7 shows how the symmetries of the solution relate to the dynamo properties of the system.

The cyclic behavior of the Taylor–Couette dynamo is related to the breaking of the equatorial symmetry of the flow induced by the growing magnetic field. Fig. 13(a) and (b) shows that the $m \neq 0$ velocity modes are maximum and not even with respect to z when the magnetic field is maximum (Fig. 13(c) and (d)). This symmetry breaking leads to the fading of dynamo action. When the magnetic energy is sufficiently low (Fig. 13(g) and (h)), the $m \neq 0$ velocity modes are small (Fig. 13(e) and (f)) and the flow is dominated by the $m = 0$ Taylor vortex flow with the adequate forcing equatorial symmetry. Dynamo action may then begin again.

4.6. Discussion

The dynamo results presented above have been obtained using a limited set of parameters. The large variety of hydrodynamic flows which may be driven in a finite Taylor–Couette set-up (including unsteady flows) opens the way to a potentially large number of dynamo studies. Moreover, the dimension of the parameter space can be increased by adding static or moving conductive solid layers around the outer cylinder, in the inner core, or on the top and bottom lids.

In the finite configuration that we have considered ($\eta = 0.5$, $\Gamma = 2\pi$, $R_e = 120$), the axial scale of the most unstable magnetic mode (with azimuthal wavenumber $m = 1$) is about twice that of the flow. This is in agreement with the periodic case,

Fig. 12. Nonlinear dynamo in the finite case. Azimuthal magnetic field at $\theta = 0$ and $\theta = \pi/2$ and azimuthal velocity field at $\theta = 0$ and $\theta = \pi/4$ without the $m = 0$ mode for $t \in \{800, 1200, 1900, 2300, 2500\}$ (a–e) and (a′–e′). The fields are normalized by the square root of the kinetic energy at $t = 2250$ and $-2 \leqslant H_\theta \leqslant 2$ (16 levels) and $-0.02 \leqslant u_\theta \leqslant 0.02$ (16 levels).

Table 7
Symmetries at various times in the finite case.

Times	Parity of H_θ	Parity of u_θ	Dynamo action
t_a, t_b	Odd	Even	Yes
t_c, t_d	Mixed	Mixed	No
t_e	Odd	Even	Yes

magnetic fields play a major role. The dynamo is cyclic in time and the fields rotate rigidly with modulated amplitude. This result shows that, even in laminar regime ($R_e = 120, R_m = 240$), realistic boundary conditions change dramatically the outcome. Assuming periodicity or enforcing realistic boundary conditions give rise to dynamos with fundamentally different behaviors.

Acknowledgments

We acknowledge fruitful discussions with L.S. Tuckerman at LIMSI and PMMH-ESPCI. JLG is thankful to University Paris Sud 11 for supporting him in June 2006 and June 2008. This work was supported by ANR project no. 06-BLAN-0363-01 "HiSpeedPIV". The implementation and parallelization of FFTW3 in the code have been made with the collaboration of Katarzyna Borońska. The computations were carried out on the IBM SP4 computer of Institut du Développement et des Ressources en Informatique Scientifique (CNRS-IDRIS) (Project # 0254).

References

[1] J. Abshagen, O. Meincke, G. Pfister, K.A. Cliffe, T. Mullin, Transient dynamics at the onset of Taylor vortices, J. Fluid Mech. 476 (2003) 335–343.
[2] A. Alonso, A mathematical justification of the low-frequency heterogeneous time-harmonic Maxwell equations, Math. Models Methods Appl. Sci. 9 (3) (1999) 475–489.
[3] T.B. Benjamin, Bifurcation phenomena in steady flows of a liquid: I. Theory, Proc. Royal Soc. London A 359 (1978) 1–26.
[4] T.B. Benjamin, Bifurcation phenomena in steady flows of a liquid: II. Experiments, Proc. Royal Soc. London A 359 (1978) 27–43.
[5] T.B. Benjamin, T. Mullin, Anomalous modes in the Taylor experiment, Proc. Royal Soc. London A 377 (1981) 221–249.
[6] C. Bernardi, M. Dauge, Y. Maday, Spectral methods for axisymmetric domains, Series in Applied Mathematics (Paris), Numerical Algorithms and Tests due to Mejdi Azaïez, vol. 3, Gauthier-Villars, Éditions Scientifiques et Médicales Elsevier, Paris, 1999.
[7] P. Boronski, L.S. Tuckerman, Poloidal–toroidal decomposition in a finite cylinder: II. Discretization, regularization and validation, J. Comput. Phys. 227 (2) (2007) 1544–1566.
[8] A. Bossavit, Computational Electromagnetism, Variational Formulations, Complementary, Edge Elements, Electromagnetism, vol. 2, Academic Press, 1998.
[9] J.H. Bramble, T.V. Kolev, J.E. Pasciak, The approximation of the Maxwell eigenvalue problem using a least-squares method, Math. Comput. 74 (252) (2005) 1575–1598 (electronic).
[10] F. Brezzi, M. Fortin, Mixed and Hybrid Finite Element Methods, Springer Series in Computational Mathematics, vol. 15, Springer-Verlag, New York, 1991.
[11] S. Chandrasekhar, Hydrodynamic and Hydromagnetic Stability, Oxford University Press, 1961.
[12] K.A. Cliffe, T. Mullin, A numerical and experimental study of anomalous modes in the Taylor experiment, J. Fluid Mech. 153 (1985) 243–258.
[13] M. Costabel, A coercive bilinear form for Maxwell's equations, J. Math. Anal. Appl. 157 (2) (1991) 527–541.
[14] J. Douglas Jr., T. Dupont, Interior Penalty Procedures for Elliptic and Parabolic Galerkin Methods, Lecture Notes in Physics, vol. 58, Springer-Verlag, Berlin, 1976.
[15] M.L. Dudley, R.W. James, Time-dependent kinematic dynamos with stationary flows, Proc. Royal Soc. London A 425 (1989) 407–429.
[16] A. Ern, J.-L. Guermond, Theory and Practice of Finite Elements, Applied Mathematical Sciences, vol. 159, Springer-Verlag, New York, 2004.
[17] M. Frigo, S.G. Johnson, The design and implementation of FFTW3, Proc. IEEE 93 (2) (2005) 216–231.
[18] J.-F. Gerbeau, C. Le Bris, T. Lelièvre, Mathematical Methods for the Magnetohydrodynamics of Liquid Metals, Numerical Mathematics and Scientific Computation, Oxford University Press, Oxford, 2006.
[19] V. Girault, P.-A. Raviart, Finite Element Methods for Navier–Stokes Equations, Springer Series in Computational Mathematics, vol. 5, Springer-Verlag, Berlin, 1986.
[20] J.-L. Guermond, Some practical implementations of projection methods for Navier–Stokes equations, Modél. Math. Anal. Num. 30 (1996) 637–667.
[21] J.-L. Guermond, R. Laguerre, J. Léorat, C. Nore, An interior penalty Galerkin method for the MHD equations in heterogeneous domains, J. Comput. Phys. 221 (1) (2007) 349–369.
[22] J.-L. Guermond, L. Quartapelle, Calculation of incompressible viscous flows by an unconditionally stable projection FEM, J. Comput. Phys. 132 (1) (1997) 12–33.
[23] J.-L. Guermond, J. Shen, On the error estimates for the rotational pressure-correction projection methods, Math. Comput. 73 (2004) 1719–1737.
[24] C.A. Jones, The transition to wavy Taylor vortices, J. Fluid Mech. 157 (1985) 135–162.
[25] P. Laure, P. Chossat, F. Daviaud, Generation of magnetic field in the Couette–Taylor system. Dynamo and dynamics, a mathematical challenge, Nato Sci. Ser. II 26 (2001) 17–24.
[26] J.M. Lopez, F. Marques, Finite aspect ratio Taylor–Couette flow: Shil'nikov dynamics of 2-tori, Physica D 211 (2005) 168–191.
[27] T. Mullin, Y. Toya, S.J. Tavener, Symmetry breaking and multiplicity of states in small aspect ratio Taylor–Couette flow, Phys. Fluids 14 (2002) 2778–2787.
[28] J. Nitsche, Über ein Variationsprinzip zur Lösung von Dirichlet-Problemen bei Verwendung von Teilräumen, die keinen Randbedingungen unterworfen sind, Abh. Math. Sem. Univ. Hamburg 36 (1971) 9–15.
[29] A.M. Rucklidge, A.R. Champneys, Boundary effects and the onset of Taylor vortices, Physica D 191 (2004) 282–296.
[30] Y. Saad, Iterative Methods for Sparse Linear Systems, PWS Publishing Company, Boston, 1996.
[31] D.D. Schnack, I. Lottati, Z. Mikić, P. Satyanarayana, A finite-volume algorithm for three-dimensional magnetohydrodynamics on an unstructured, adaptive grid in axially symmetric geometry, J. Comput. Phys. 140 (1) (1998) 71–121.
[32] M. Sermange, R. Temam, Some mathematical questions related to the MHD equations, Commun. Pure Appl. Math. 36 (5) (1983) 635–664.
[33] C.R. Sovinec, A.H. Glasser, T.A. Gianakon, D.C. Barnes, R.A. Nebel, S.E. Kruger, S.J. Plimpton, A. Tarditi, M.S. Chu, the NIMROD Team, Nonlinear magnetohydrodynamics with high-order finite elements, J. Comput. Phys. 195 (2004) 355.
[34] R. Tagg, The Couette–Taylor problem, Nonlinear Sci. Today 4 (3) (1994) 1–25.
[35] G.I. Taylor, Stability of a viscous liquid contained between two rotating cylinders, Philos. Trans. Royal Soc. London A 223 (1923) 289–343.
[36] R. Temam, Navier–Stokes Equations, Studies in Mathematics and its Applications, vol. 2, North-Holland, 1977.
[37] L.J.P. Timmermans, P.D. Minev, F.N. van de Vosse, An approximate projection scheme for incompressible flow using spectral elements, Int. J. Numer. Methods Fluids 22 (1996) 673–688.
[38] A.P. Willis, C.F. Barenghi, A Taylor–Couette dynamo, Astron. Astrophys. 393 (2002) 339–343.
[39] A.J. Youd, C.F. Barenghi, A.P. Willis, Hydromagnetic instabilities in Taylor–Couette flow at finite and infinite aspect ratio, AIP Conference Proceedings, editor, MHD Couette Flows: Experiments and Models, vol. 733, Academic Press, New York, 2004, pp. 83–99.